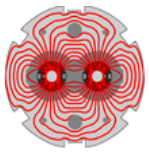

LHC Performance Note-014

2009-12-21

Alan.Fisher@cern.ch

Expected Performance of the LHC Synchrotron-Light Telescope (BSRT) and Abort-Gap Monitor (BSRA)*

Alan S. Fisher / BE-BI†

BSRT, BSRA, synchrotron light, undulator, abort gap, heavy ions

Summary

This Report presents calculations of the synchrotron light from proton and lead-ion beams in the LHC at all energies from 0.45 to 7 TeV. It computes the emission from three sources: the uniform-field region of the D3 dipole, the dipole's edge field, and the short undulator just upstream. Light emitted at or near visible wavelengths is assessed for making optical measurements of transverse beam profiles and for monitoring the emptiness of the abort gap in the fill pattern. There is sufficient light for both applications, although both species pass through energy ranges in the ramp with small photon counts. Effects limiting image resolution are examined, including geometric optics, depth of field, and diffraction.

The Report also considers recent suggestions that the undulator, intended to supplement the dipole for low energies, should not be ramped off at high energies and perhaps should not be used at all. We conclude that the undulator is essential at low energy for both species, but that it is possible to leave the undulator on at the cost of some blurring at intermediate energies.

1 Introduction

This Report calculates the expected performance of two diagnostic applications of the LHC synchrotron-light telescope. The BSRT [1] measures the transverse beam size. The BSRA [2] monitors the population of the 3-μs beam-abort gap in the fill pattern, since the rise of the abort kicker may drive particles there into a magnet and cause a quench.

1.1 Dipole and Undulator

The BSRT images the proton beams with video cameras. Two sources of visible synchrotron emission from each beam span the full range of proton energies. The primary source is the D3 dipole, one of a set of four 9.45-m-long superconducting dipoles that separate the beams on either side of the RF cavities at Point 4. These magnets ramp to a maximum field B_d (corresponding to 7-TeV protons) of 3.90 T, giving a bend angle of 1.58 mrad and a radius of curvature ρ = 6013 m. At a distance of 26 m downstream of the D3 entrance, the

* This work was supported by the United States Department of Energy through the US LHC Accelerator Research Program (LARP).

† Permanent address: SLAC National Accelerator Laboratory, Menlo Park, California, USA.

protons are sufficiently separated from the photons to provide room for a mirror that extracts the light, directing it downward to optics in a shielded enclave below the beamline.

At injection energy, the dipole provides far too little visible light for measurement. Consequently, a short superconducting undulator [3] with two 28-cm periods is inserted upstream of D3 in the same cryostat, with a 937-mm gap between magnets. With a field of $B_u = 5$ T, its spectrum peaks in the red (610 nm) for 450-GeV protons, providing visible light at injection.

Unlike the dipole, the undulator field remains constant during the energy ramp. Once the proton energy rises above 2 TeV, the original intention was to ramp the undulator off, since its peak emission is then strongly shifted to shorter wavelengths while the dipole offers significant output in the visible. Also, at intermediate energies where both sources produce visible light, image blur is a concern, since the imaging system cannot be focused on both.

More recently, concerns have been raised that one undulator has a faulty resistor inside the cryostat. This resistance helps to match the magnet's power supply to drive its inductive load, and so its ability to ramp could be limited by the fault. The resulting questions—whether the undulator is truly required, and, if so, is it necessary to ramp it off at higher proton energies—are addressed in this Report.

1.2 Heavy Ions

Some portion of LHC operations will involve collisions of lead ions (^{208}Pb) rather than protons. The planned number of bunches and bunch populations are smaller, and the emission spectrum is shifted to longer wavelengths. Thus operation with heavy ions requires a separate evaluation of the signal strength. In particular, it is important to determine if there is sufficient signal to monitor the abort gap at injection.

A particle with charge Ze and momentum p in a dipole field B curves with a radius $\rho = p/(ZeB)$. Any particle orbiting in the ring follows this radius, and so its momentum must scale with ZB. As the dipole ramps to its maximum field, protons ramp from 0.45 to 7 TeV. Lead ions, with $Z = 82$, must then ramp from 37 up to 574 TeV, equal to 100 μJ *per ion*. (The ion energy will frequently be expressed in terms of the "equivalent proton energy" at the corresponding point in the ramp.) To highlight the effects of the different mass and charge, we define $A = m_{\mathrm{Pb}}/m_{\mathrm{p}} = 206.43$ (an admittedly nonstandard usage). The relativistic factor γ and the energy per nucleon scale by Z/A, giving ions with 2.76 TeV/nucleon at the top of the ramp.

2 Energy Distribution in Angle and Frequency, per Particle and per Turn

This section provides analytic expressions for the power radiated in the undulator and dipole. All cases include a sum of two terms, for the horizontal and vertical polarizations respectively, but we mostly use only the total. Separate expressions are provided for emission from the edge and centre of the dipole. These calculations agree well with those in [1] for comparable bandwidths and extraction geometry.

We are interested in the energy emitted by one particle of charge $q = Ze$ and mass $m = Am_p$ into a solid angle $d\Omega$ and a bandwidth $d\omega$. Because the extraction mirror is rectangular, it is helpful to write $d\Omega$ in terms of the transverse horizontal angle ξ and vertical angle ψ, both of which we normalize to the characteristic emission angle $1/\gamma$. Expressions for the energy $W(\xi,\psi,\omega,\gamma)$ emitted into $d\xi\, d\psi\, d\omega = \gamma^2 d\Omega\, d\omega$ are given in the following subsections.

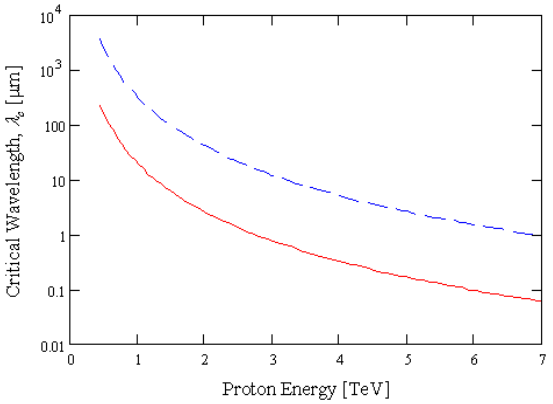

Figure 1. Critical wavelength in the D3 dipole for protons (solid red) and lead ions (dashed blue) vs. proton energy (or the equivalent point in the ramp for ions).

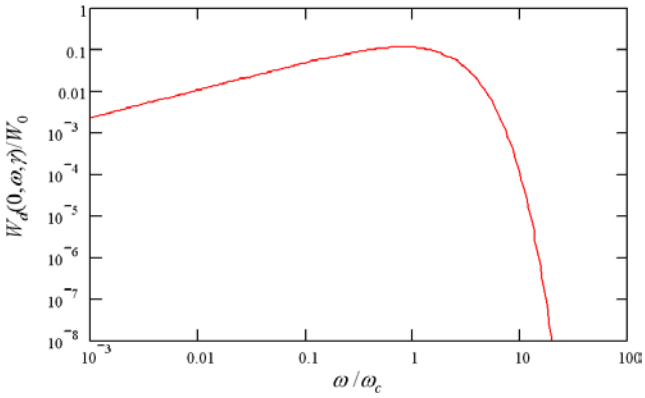

Figure 2. Spectrum of on-axis radiation from the central field of a dipole, versus the normalized frequency $\varepsilon = \omega/\omega_c$.

2.1 Radiation from the Central Field of a Dipole

Expressions for radiation by a charged particle following a circular orbit with radius ρ in a uniform field B_d may be found in many references, such as Hofmann [4] or the convenient x-ray booklet [5]. The expression assumes a "long magnet"; that is, the curved path L_d is long enough for the full emission cone to sweep across a distant observer. This requires a bend angle comparable to the full opening angle ($\approx 1/\gamma$), or $L_d \gg \rho/\gamma$, a criterion that is satisfied for the energies at which central radiation will be used. We define the critical frequency ω_c (along with the critical energy $E_c = \hbar\omega_c$ and wavelength $\lambda_c = 2\pi c/\omega_c$):

$$\omega_c = \frac{3}{2}\gamma^3 \frac{c}{\rho} \tag{1}$$

Figure 1 shows the variation in critical wavelength through the energy ramp. The energy radiated per particle into $d\xi\, d\psi\, d\omega$ is independent of the horizontal angle ξ (in the plane of the bend). It is expressed using modified Bessel functions $K_\nu(\zeta)$:

$$W_d(\psi,\omega,\gamma) = Z^2 \frac{3}{4\pi^2} W_0 \left(\frac{\omega}{\omega_c}\right)^2 \left(1+\psi^2\right)^2 \left[K_{2/3}^2(\zeta) + \frac{\psi^2}{1+\psi^2} K_{1/3}^2(\zeta)\right] \tag{2}$$

$$\zeta = \frac{\omega}{2\omega_c}\left(1+\psi^2\right)^{3/2} \tag{3}$$

$$W_0 = \frac{e^2}{4\pi\varepsilon_0 c} = 7.6956\cdot 10^{-37}\ \mathrm{J\cdot s} \tag{4}$$

The first term inside the square brackets of (2) is for horizontal polarization, and the second is for vertical. Figure 2 shows the spectrum on axis ($\xi = \psi = 0$), which peaks at the critical frequency and then drops sharply. Comparing this drop to Figure 1, we see that there is little central radiation emitted in the visible at injection.

2.2 Radiation from the Edge Field of a Dipole

The short passage of a particle through the dipole's edge field shifts the spectrum to higher frequencies. For this reason, edge radiation was proposed as the primary source of light for the BSRT [1]. The expression for the energy radiated by a particle passing through the edge field is given by Coïsson [6] for the case of an edge field that rises like an arctangent:

$$B(z) = \frac{B_d}{2}\left(1 + \frac{2}{\pi}\arctan\frac{z}{L_e}\right) \tag{5}$$

After converting the angle coordinates to ξ and ψ, Coïsson's expression for the radiated energy in both polarizations may be rewritten in the form:

$$W_e(\xi,\psi,\omega,\gamma) = Z^2\frac{8}{9\pi^2}W_0\left(\frac{\omega_c}{\omega}\right)^2\frac{\left(1-\xi^2+\psi^2\right)^2+\left(2\xi\psi\right)^2}{\left(1+\xi^2+\psi^2\right)^6}\exp\left[-\frac{\omega L_e}{\gamma^2 c}\left(1+\xi^2+\psi^2\right)\right] \tag{6}$$

There are two difficulties with the use of edge radiation. Section 3 will show that at high beam energies, this emission has a very narrow angular pattern, which leads to significant diffraction that broadens the measured beam size, as will be discussed in Section 6.

A hint of a more fundamental difficulty lies in the spectral dependence of (6), which diverges at low frequencies and has an infinite integral. Coïsson notes that this expression is only meaningful for $\omega \gg \omega_c$, since the derivation assumes that the time over which an observer receives edge radiation, $L_e/(2\gamma^2 c)$, is short compared to $1/\omega_c$, characteristic of central radiation. This is equivalent to assuming a short edge: $L_e \ll \rho/\gamma$. At lower frequencies it is not appropriate to separate edge from centre, and the ω^{-2} divergence of the emitted energy can be neglected.

The calculations below will continue using (6), but for proton energies above 3 TeV, Figure 1 shows that λ_c enters the visible, and so this expression gives at best an upper bound on the energy detected. For lead ions, on the other hand, since λ_c enters the visible just above 7 TeV, the expression remains valid over the full energy range.

2.3 Radiation from the Undulator

The undulator has N_u = 2 periods of length λ_u = 28 cm, and corresponding wavenumber $k_u = 2\pi c/\lambda_u$. As the beam energy ramps, the peak on-axis field B_u is held constant, until the undulator is perhaps ramped off when the dipole radiation is sufficient. We define the undulator parameter K_u:

$$K_u = \frac{ZeB_u}{Am_p ck_u} = \frac{Z}{A}K_{up} \tag{7}$$

Here K_{up} is the undulator parameter for protons. When $K_u << 1$, as it is here, relativistic particles ($\gamma >> 1$) have their first-harmonic peak for angles ξ and ψ at frequency:

$$\omega_1(\xi,\psi,\gamma) = \frac{2\gamma^2 ck_u}{1+\xi^2+\psi^2} \tag{8}$$

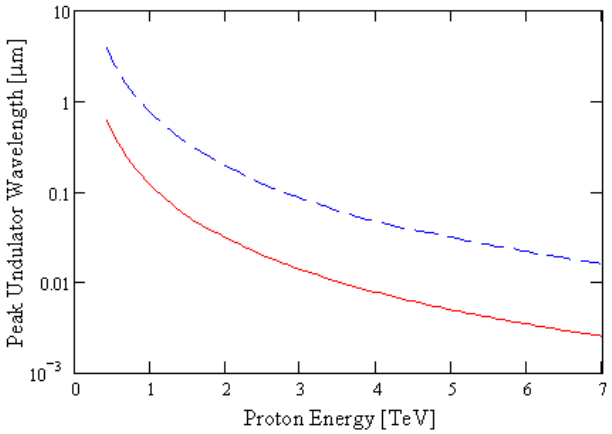

Figure 3. Peak on-axis emission wavelength in the undulator for protons (solid red) and lead ions (dashed blue) vs. proton energy (or the equivalent point in the ramp for ions).

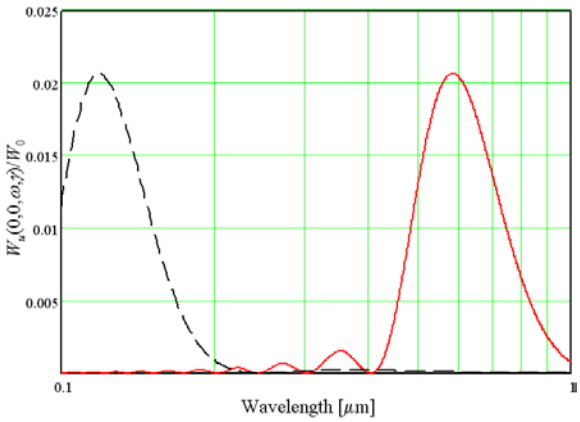

Figure 4. Proton emission spectrum on axis versus wavelength (log scale) from the undulator at injection (solid red) and 1 TeV (dashed black).

This corresponds to a peak wavelength of:

$$\lambda_1(\xi,\psi,\gamma) = \lambda_u \frac{1+\xi^2+\psi^2}{2\gamma^2} \tag{9}$$

The energy per particle emitted into $d\xi\, d\psi\, d\omega$ is given by Hofmann [4]:

$$W_u(\xi,\psi,\omega,\gamma) = \frac{Z^4}{A^2} N_u^2 K_{up}^2 W_0 \frac{\left(1-\xi^2+\psi^2\right)^2+\left(2\xi\psi\right)^2}{\left(1+\xi^2+\psi^2\right)^4} f_\omega(\xi,\psi,\omega,\gamma) \tag{10}$$

$$f_\omega(\xi,\psi,\omega,\gamma) = \left(\frac{2\omega}{\omega+\omega_1}\right)^2 \mathrm{sinc}^2\left(\pi N_u \frac{\omega-\omega_1}{\omega_1}\right) \tag{11}$$

Figure 3 shows that the peak wavelength for on-axis radiation from protons at injection energy is 609 nm, but is 3.86 μm for lead ions. At maximum energy, the proton emission peaks at 2.52 nm, compared to 16.0 nm for lead ions. Figure 4 shows that the proton spectrum on axis, using Eq. (10), lies largely in the visible at injection (0.45 TeV), while at 1 TeV almost all the radiation has moved into the near ultraviolet.

The second factor (sinc^2) in the spectral dependence (11) leads, for $N_u >> 1$, to a narrow bandwidth of order $1/N_u$ centred at the peak frequency ω_1. At frequencies where this second factor is significant, the first factor is very close to 1 and so is generally omitted. For example, Ref. [4] keeps this factor in Eq. (7.29) for the electric field, but then discards it in Eq. (7.35) for the energy. However, we shall see that at higher beam energies, for which the emission peaks at frequencies well above the visible, this "short-undulator" factor has a significant effect in suppressing a false peak in the visible tail, and so it must be retained for a correct calculation of the energy entering the optical system.

3 Distribution of Light on the Extraction Mirror

This section compares the distribution of light on the extraction mirror from these three sources at different proton energies. We integrate the distributions in angle and frequency over

a frequency band $\omega_b - \omega_a$ that is a bit wider than that of a typical camera—including the visible, the near infrared, and near ultraviolet:

$$\omega_a = \frac{2\pi c}{900\,\text{nm}} \qquad\qquad \omega_b = \frac{2\pi c}{200\,\text{nm}} \tag{12}$$

Section 7.2 will narrow this bandwidth to that of the real LHC camera, and include its wavelength-dependent sensitivity. Section 7.3 will integrate twice more, over the angles that span the mirror surface, to find the total energy on the mirror.

We place the origin of our *xyz* coordinates at the entrance edge of D3, in the middle of the rise of the field, which is $z = 0$ in Eq. (5). The particles travel in the $+z$ direction. The $+y$ direction is vertically upward. The radially outward direction is $+x$. For beam 1, which travels clockwise around the ring, this forms a right-handed coordinate system. The distance along the beam's curved orbit is called *s*, with $s = 0$ at $z = 0$.

The undulator ends at $z = -937$ mm. Following Hofmann [4], we compute the undulator radiation from the centre of the undulator, at $z = -1\,217$ mm. The dipole's central (uniform-field) radiation follows the tangent to the orbit. As the particle enters the dipole, the light first strikes the extraction mirror at $x = 0$ and then sweeps toward $-x$ until the tangent misses the mirror when the particle passes $z = 3.2$ m. The extraction mirror is at $z = 26.023$ m.

The mirror is square, 40 mm on each side, but to provide a larger clearance to the proton or ion beam, it is offset toward $+x$. The mirror is rotated by 45° about the *x* axis in order to direct the reflected light vertically downward to the optical table. The mirror edges are at coordinates:

$$\begin{aligned} x_a &= -13\,\text{mm} \quad \text{to} \quad x_b = 27\,\text{mm} \\ y_a &= \frac{-20\,\text{mm}}{\sqrt{2}} \quad \text{to} \quad y_b = \frac{20\,\text{mm}}{\sqrt{2}} \end{aligned} \tag{13}$$

3.1 Protons at 7 TeV

Figure 5 shows the radiation distribution on the surface of the extraction mirror, for light emitted within the band (12) by 7-TeV protons in (a) the dipole centre, (b) the dipole edge, and (c) the undulator. The vertical scales are all normalized to $(\omega_b - \omega_a)W_0$.

Figure 5(a) shows a hard edge at $x = 0$ on the mirror from central radiation. This is not physical: Eq. (2) describes radiation from the middle of a long magnet but not its edge. Near $x = 0$, the emission should roll off with the opening angle discussed in Section 5.3.

Figure 5(b) shows edge radiation calculated from Eq. (6). The horizontal and vertical widths of only 37 and 60 μrad RMS are clearly far narrower than the central radiation in (a). Section 6 will show that these narrow angles lead to significant diffractive broadening of beam measurements. The integrated magnitudes from the edge and centre are similar, as will be seen shortly.

We have somewhat artificially separated edge from central radiation to highlight their different spectral properties. Recall, though, from Section 2.2 that at this beam energy, where $\omega >> \omega_c$, Eq. (6) diverges and this separation of edge and centre is inappropriate.

The undulator radiation in this band, shown in Figure 5(c), is seven orders of magnitude smaller, and at a minimum at the origin.

3.2 Protons at 450 GeV

At injection, the situation is reversed. Figure 6 shows that the dipole centre emits zero in the band given by (12) (within the computer's tolerance). Both the undulator and the dipole edge emit broad peaks that are a bit wider than the mirror, but the undulator radiation is five orders of magnitude larger. The vertical scales are again normalized to $(\omega_b - \omega_a)W_0$.

3.3 Protons at 1.5 TeV

At intermediate energies, the strongest source gradually shifts from the undulator to the dipole, and so the question of blurring due to multiple sources arises. Figure 7(a) and (b) suggests that at 1.5 TeV the proton radiation is comparable in band (12) from the dipole's edge and centre. We can reduce the blurring from multiple sources by placing a horizontal slit (a slit that opens in x and has its long axis along y) on the optical table at a distance of one focal length from the first focusing mirror. The slit (see Section 5.2) transmits light as a function of the horizontal angle ξ on the source plane and so can be set to select a range of source points.

If the slit passes edge radiation, then undulator radiation, which is also emitted parallel to z, must also go through. This third source is at a different distance and so leads to additional blurring. The simplest remedy

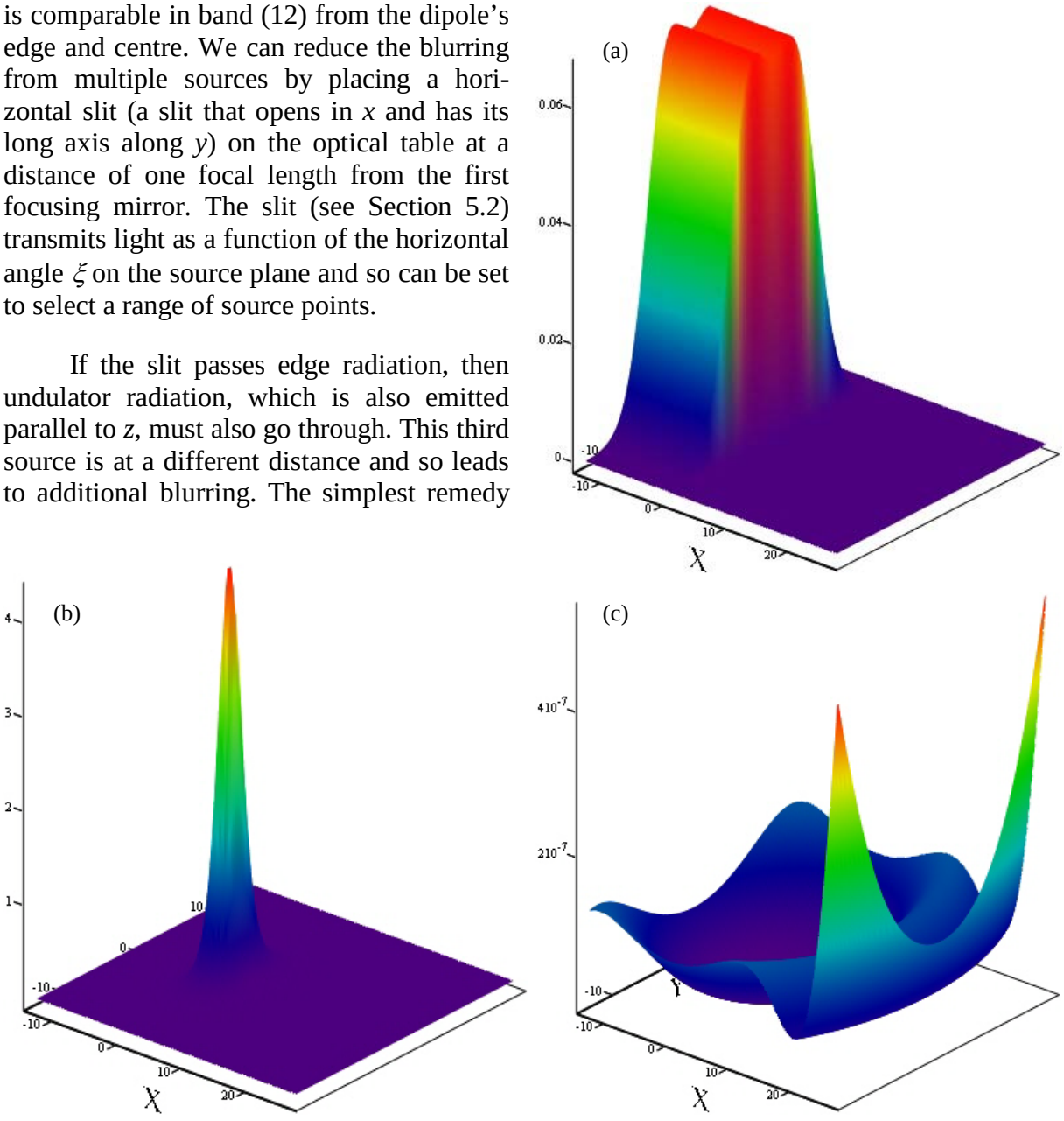

Figure 5. Radiation on the extraction mirror between 200 and 900 nm emitted by 7-TeV protons: (a) from dipole centre, (b) from dipole edge, and (c) from undulator. The vertical scales are normalized to $(\omega_b - \omega_a)W_0$. The undulator light is lower the other sources by 10^7.

would be to shut the undulator off at this point in the ramp.

Whether the undulator should be ramped off depends on the emitted energy it sends to the mirror compared to the other sources. First this energy must be calculated properly. Figure 7(c) and (d) compare two computations of the undulator radiation. The full expression of Eq. (11) for the spectral dependence is used in (c), while (d) omits the first factor, as is commonly done for undulators with many periods. At this proton energy, the peak emission wavelength on axis is 55 nm. For our far longer wavelengths near the visible, the factor's main effect is suppression of the wide central peak in (d), one that would otherwise be sufficiently strong to be the dominant contribution. We look next at the energy on the mirror and return to the effect of leaving the undulator on in Section 7.3.

3.4 Comparison of Energy per Proton on the Extraction Mirror

Figure 8 plots the total radiated energy per proton, within the bandwidth of Eq. (12) and collected by the extraction mirror, as a function of proton energy. Undulator radiation dominates below 1 TeV, with a peak near 0.7 TeV in this band. Above 2 TeV, the dipole's central radiation is dominant. Blurring is expected only in the narrow region where all three sources contribute roughly equal light. (The exact location of this crossing depends on the wavelength response of the optics and camera, which is discussed in Section 7.2.) At high beam energies, there is little interference in the visible if undulator is left on.

In Figure 8, radiation from the dipole

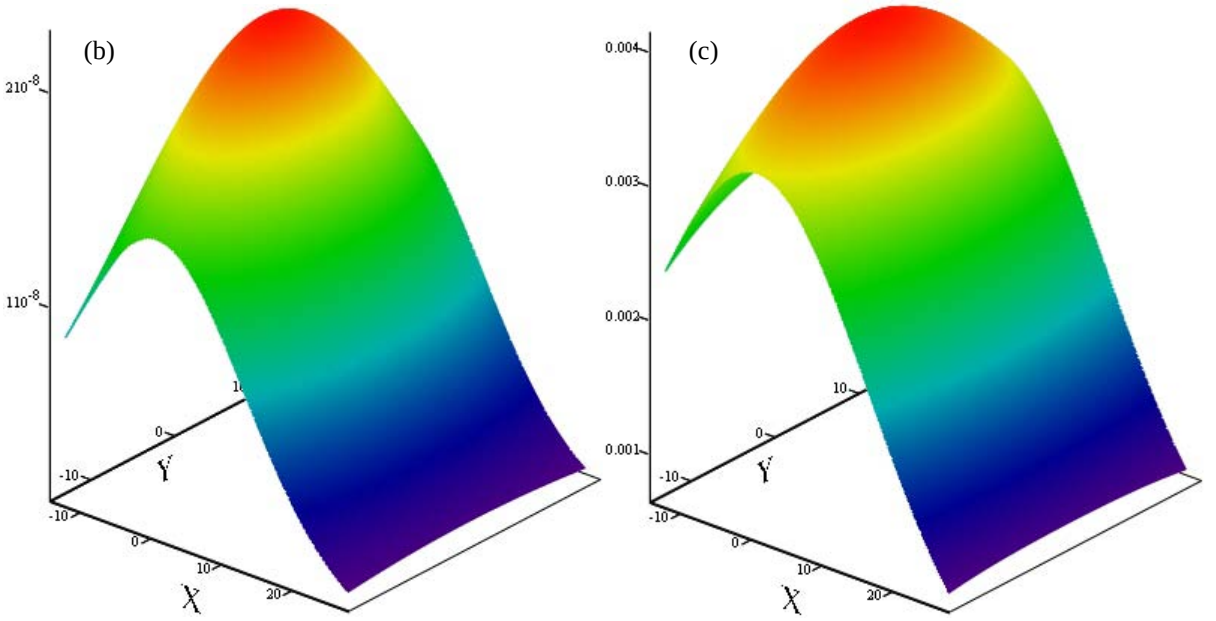

Figure 6. Radiation on the extraction mirror between 200 and 900 nm emitted by 450-GeV protons: (a) from dipole centre, (b) from dipole edge, and (c) from undulator. The vertical scales are normalized to $(\omega_b - \omega_a)W_0$. The dipole centre gives zero, while the edge contribution is 10^5 times below that of the undulator.

edge exceeds that from the centre for proton energies above 5.5 TeV. However, Section 2.2 pointed out that the expression for edge radiation diverges when $\omega_c >> \omega$, and so it provides only an upper bound above 3 TeV.

3.5 Undulator X-Ray Power on the Extraction Mirror

Figure 8 shows that the undulator emission in the band (12) drops off significantly at high beam energies. However, the total power it radiates rises with the square of the energy. This power moves out of band and into the x-ray region, striking the mirror in a spot of about 1-mm diameter. This is an unnecessary heat load on the extraction mirror, since we do not make use of this radiation. Is it large enough to require turning the undulator off?

A full ring has 2808 bunches of 1.1×10^{11} protons, or 592 bunches of 7×10^{7} ions. As

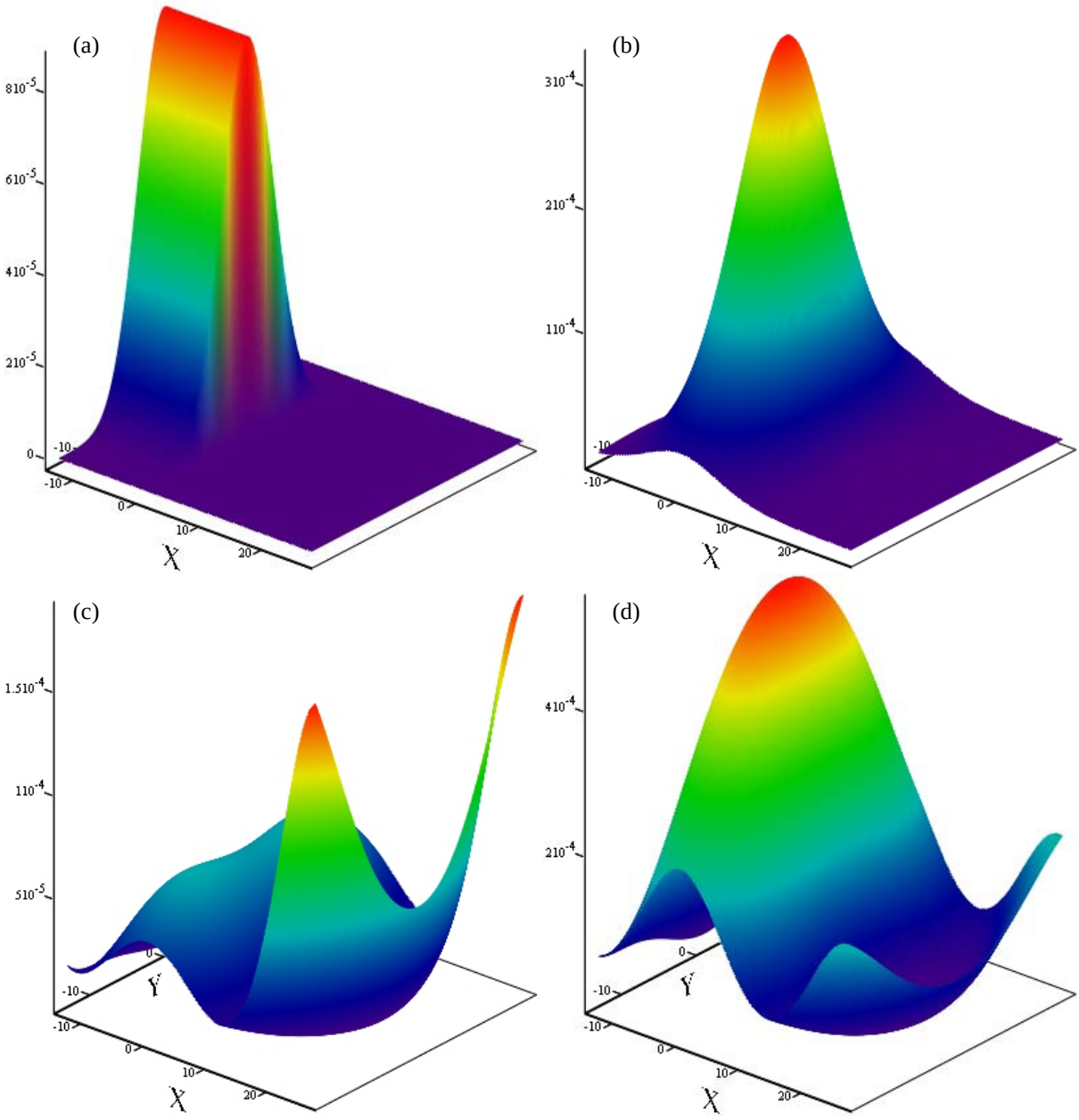

Figure 7. Radiation on the extraction mirror between 200 and 900 nm emitted by 1.5-TeV protons: (a) from dipole centre; (b) from dipole edge; (c) from undulator; and (d) from undulator, but without the "short-undulator" factor. Omitting this factor in (d) adds a false central peak. The vertical scales are normalized to $(\omega_b-\omega_a)W_0$.

each particle makes a single pass through the undulator, it radiates a total energy given by Eq. (7.32) of Ref. [4]:

$$W_{u,tot} = \frac{Z^4}{A^2}\frac{2\pi}{3} W_0 c k_u \gamma^2 K_u^2 N_u \tag{14}$$

The metal-coated silicon extraction mirror receives a total heat load of 21 mW from a full ring of protons at maximum energy, and only 0.5 mW from a full ring of ions. Since the mirror has no active cooling, its temperature rise depends on whether it is cooled radiatively or by conduction through the mount, which is a shaft extending from a linear vacuum feedthrough. Nevertheless, a simple analysis shows that conduction within the silicon spreads this small power nearly uniformly over the full surface of the mirror. Then radiation and whatever conduction is available are sufficient to avoid any significant temperature rise.

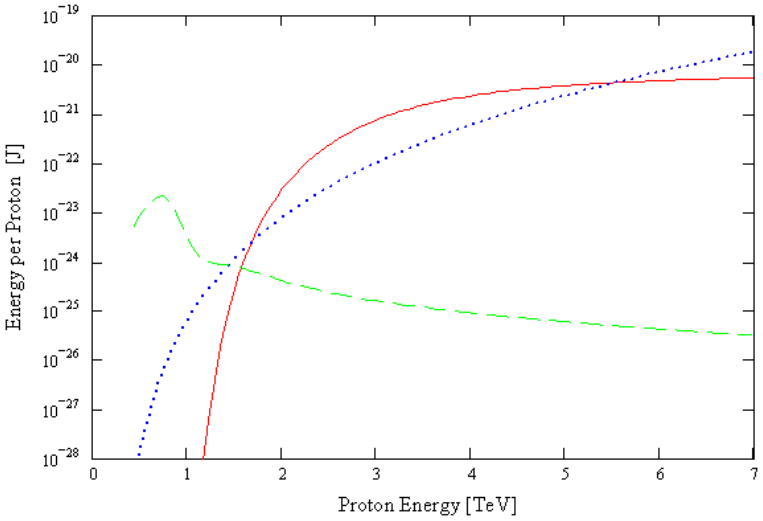

Figure 8. Radiated energy per proton collected by the extraction mirror, from the dipole centre (solid red), the dipole edge (dotted blue), and the undulator (dashed green), for wavelengths between 200 and 900 nm.

4 Imaging Optics

The optical system is highly constrained by the layout of the LHC. The 1.6-mrad bend angle of the dipoles demands a long drift distance—26.023 m—from D3 to the extraction mirror, in order to separate protons from photons. The drift is larger, 27.240 m, when the source is the middle of the undulator. The light then passes downward through a fused-silica vacuum window to imaging optics below the beamline. Consequently, the distance to the first focusing optic F1 is 32 m, which certainly justifies including "telescope" in the system's name, BSRT (beam synchrotron-radiation telescope).

The optical systems for the LHC beams were originally designed to reuse the two cylindrical tanks that housed synchrotron-light monitors for LEP. The optical components inside each tank are mounted on the top and sides of an optical rail. However, both tanks have recently been replaced with optical tables, laid out as shown in Figure 9. The additional space allowed us to add the focusing "trombone" delay line and calibration path shown in the figure and discussed below. The table dimensions, 4.8×0.8 m^2, are determined by the available space

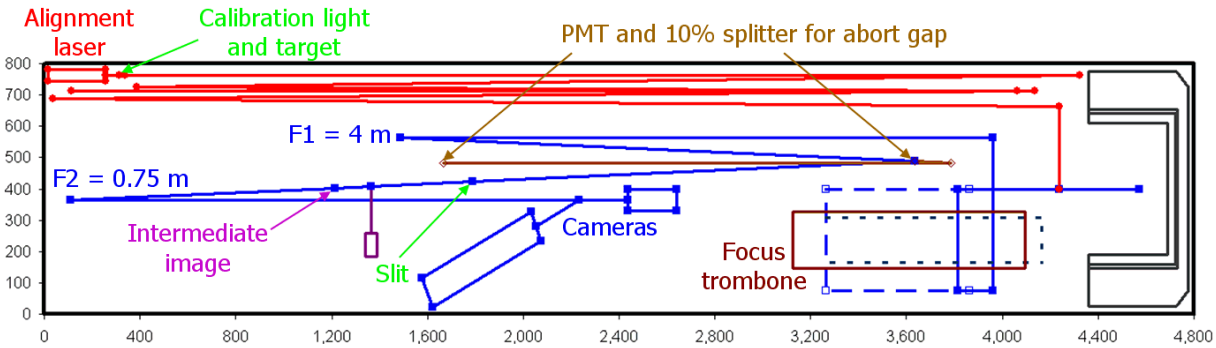

Figure 9. Layout of the optical table. Table coordinates are in mm.

under the beamline.

Due to the long distance from the source, spherical mirror F1 must demagnify in order to form an image on the table. A second, magnifying stage, F2, is then needed to produce an image compatible with the pixel spacing of the cameras (or, for an intensified camera, the pixels imaged to the photocathode). The Proxicam intensified camera for LHC (Section 7.2) has an effective pixel spacing of 16.5 μm. Excessive magnification should also be avoided, since the injected beam is larger and since the available light can spread over too many pixels, leading to noise. The overall magnification of 0.3 images 7-TeV protons to a typical size of 100 μm RMS, and 450-GeV protons to 300 μm.

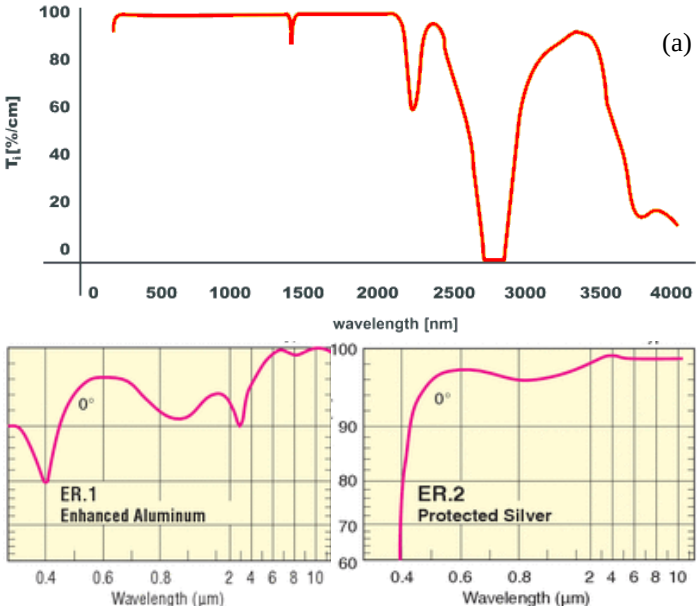

Figure 10. (a) Transmission of the fused-silica vacuum window, (b) typical reflectivity for protected aluminium (coating the F1 mirror), and (c) reflectivity of protected silver (coating F2).

The design requires broadband optics, because the spectrum varies with the different sources, beam energies, and particle types. Thus reflective rather than refractive optics are preferable. The bandpass is limited in the infrared by the transmission of the fused-silica window (Figure 10(a)), and in the ultraviolet by reflectivity of the metal mirror coatings. The F1 and F2 mirrors, previously acquired by CERN, have different coatings: F1 uses protected aluminium (Figure 10(b)), while F2 uses protected silver (Figure 10(c)); both are applied to Zerodur substrates. These are spherical concave mirrors with radii of curvature of 8000 and 1500 mm respectively, corresponding to focal lengths of 4000 and 750 mm.

To minimize geometric aberrations, the light is incident on both focusing mirrors at only 1° to the normal in the horizontal plane. Figure 11 shows "spot" diagrams (point-spread functions) computed by ZEMAX optics software [7]. It shows images of three points, one on axis, and two displaced by 1 mm in x and y respectively. All three

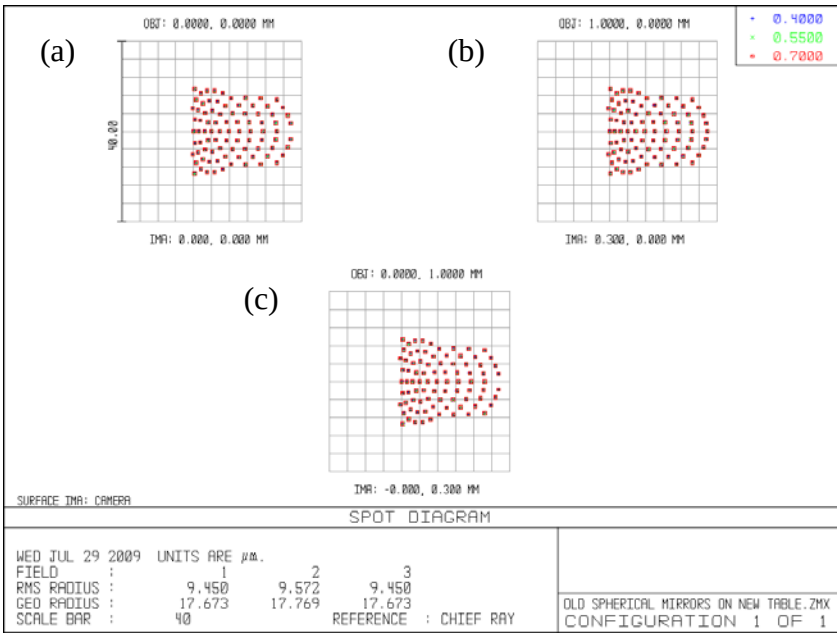

Figure 11. ZEMAX spot diagram showing the 16-μm RMS spread of images of three source points, at: (a) x=y=0 (on axis); (b) x=1 mm, y=0; and (c) x=0, y=1 mm. The grids are 10 μm/division, 100 μm full scale. Red, green and blue rays nearly overlap, showing little chromaticity.

points blur on the camera to 9.5 μm RMS. The small size of the extraction mirror clips rays farthest from the axis, reducing the blurring from spherical aberration. However, the broad ray pattern used by ZEMAX is more subject to clipping than the narrow emission pattern of our sources (as shown in Figure 5 through Figure 7). The three ray colours traced overlap almost perfectly, thanks to reflective optics. The only chromatic component, the window, has little effect, because it is flat and struck at normal incidence.

Recently the optical system was assembled and tested in the lab. It was found that the original F1 mirrors are too thin, with the result that tension applied by the mount significantly distorts the image. New F1 mirrors with better specifications and with silver coatings have been ordered. The remainder of the system appeared to perform properly when a mirror with a shorter focal length was substituted for F1, but a full system test awaits the new mirrors.

A design using off-axis elliptical mirrors was developed to improve on these spherical optics. Since any portion of the surface of an ellipse has perfect geometric imaging from one focus to the other, elliptical mirrors can be devised for any angle of incidence. A ZEMAX spot diagram with the same three source points finds spreads below 1 μm RMS (and 0 μm for the on-axis point without a window). However, such mirrors are costly, and the geometric blurring from spherical optics contributes less to the ultimate resolution than diffraction (Section 6). Elliptical optics may be considered in the future as an upgrade.

Since the light source shifts by up to 2.8 m during the ramp—from the middle of the undulator to 1.6 m inside D3—the optical focus must move too. Adjusting it by moving a mirror is difficult with off-axis reflective optics, since translation would also steer the reflection. Instead, an optical-trombone delay line (Figure 9) before F1 maintains a constant optical path and magnification. A 600-mm motorized translation stage in a 2-pass configuration (dashed blue lines in the figure) gives delays of up to 1200 mm. For longer delays of up to 3 m, a short stage inserts two more mirrors into the light path on the moving platform, making a double trombone with four passes (short black dashes) including two additional fixed mirrors on the table. The 4-pass delay is needed to focus inside the dipole and at its entrance.

The new calibration path includes an alignment laser with a divergence similar to the light from the proton beam, and an incoherently illuminated resolution target. Multiple passes across the table give this line the same length as the optical path from the undulator.

Before reaching F1, the light reflects from the extraction mirror, from a mirror below the vacuum window that redirects the light onto the optical table, and from 4 or 8 trombone mirrors. The mirror surfaces are coated with either silver or aluminium. The exact reflectivity spectra are not available for all these mirrors, but some silver coatings can extend beyond the 400-nm cut-off of Figure 10(b) to 350 nm. We simplify the analysis of the reflection loss by assuming a hard edge at 380 nm in the ultraviolet, a fixed reflectivity of 96% through the visible and as far as the infrared cut-off of the vacuum viewport. The accumulated losses result in mirror transmissions (within this band) of 65% and 55%, for the 2-pass and 4-pass trombones respectively.

To monitor whether the abort gap in the fill pattern is sufficiently empty of protons or ions, 10% of the light between F1 and F2 is picked off by a partially transmitting mirror. In this split beam, a photomultiplier (Figure 9) is placed at the intermediate image formed by F1. This monitor will be considered in Section 8.

5 Modelling an Extended Source

For the first 3.2 m of the beam orbit in the central region of the dipole, rays tangent to the orbit intercept the extraction mirror and so may contribute to the image. Further inside, the tangents miss the mirror's edge. The diffraction considerations touched on earlier (and discussed in detail in Section 6) suggest that it is helpful to use the longest path, in order to broaden the horizontal angular range. But such an extended source may blur the image due to the limited depth of field of the optics.

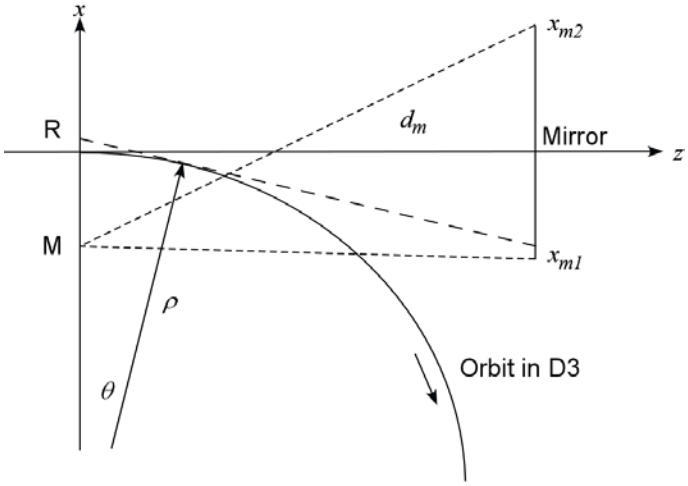

Figure 12. Radiation from a point on the orbit inside the D3 dipole.

5.1 Orbit in the *xz* Plane

Figure 12 shows a proton orbit inside the dipole (with an exaggerated bend angle). The origin is the middle of the entrance plane, at $z = 0$ in Eq. (5). If the optical system is focused on this plane, then a ray emitted along the tangent appears equivalent in the image to one originating at point R on the x axis. For points on the orbit, the relationship between the emission angle θ and the apparent emission point x is:

$$x = \rho(1/\cos\theta - 1) \approx \tfrac{1}{2}\rho\theta^2 \tag{15}$$

Similarly, for a point M on the x axis, we can find the largest and smallest angles of rays that hit the extraction mirror. These observations allows us to describe the xx' phase space (where $x' = \theta$) of all the rays emitted as the beam travels through the dipole.

5.2 Acceptance in *xx′* Phase Space

Figure 13 displays the information from the previous section in phase space. The rays emitted along the orbit are shown as the parabola of Eq. (15), but only for $x' < 0$, since the angle is zero at the dipole entrance and the bend is toward negative angles. Similarly, the plot shows two lines giving the xx' relationships for rays hitting the left and right edges of the mirror; these lines define the mirror's acceptance.

The magenta lines in Figure 13 show the slit introduced in Section 3.3. Placed at one focal length from the first focusing mirror, the slit passes the same range of angles x' for any x, and so its edges form horizontal lines. In the figure the lines are shown at angles corresponding to the tangents to the orbit at $s = 10$ and 300 cm. The slit can be set to favour central or edge radiation. However, because undulator and edge radiation both enter with angles centred about $x' = 0$, a slit cannot aid in distinguishing these sources.

The 1-sigma phase-space ellipse of a 7-TeV proton beam is shown at three different places along the orbit. There is a significant displacement of these ellipses in x before the orbit crosses the line of the mirror edge. A composite x distribution from a range of points along the path can be formed by projecting these ellipses onto the x axis. As the slit widens to incorporate a longer path, the combined distribution widens as well and shifts steadily rightward. However, this analysis involves only the distribution of the protons. We next focus on our real concern, which is the distribution of the light they emit.

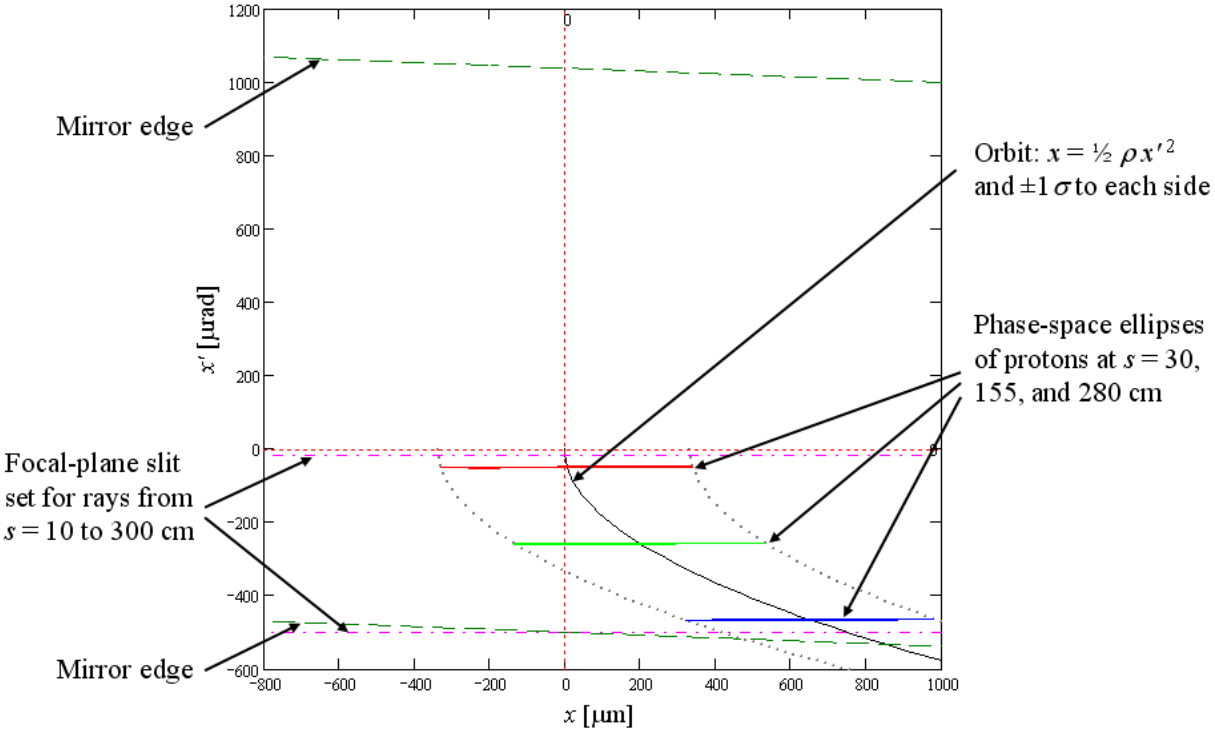

Figure 13. Horizontal phase space for emission in the dipole, with the coordinates and the optical focus in the plane of the dipole entrance. The very thin ellipses show the proton phase space at three points along the orbit, transported to the entrance plane.

5.3 The *xx'* Phase Space of the Light

Radiation from all three sources considered here is emitted along the direction of the particle beam in a narrow cone. The characteristic cone angle is of order $1/\gamma$ for wavelengths near the emission peak, but this can be misleading for wavelengths in the tail. For a uniform dipole field, the RMS opening angle of the radiation is approximated by [5]:

$$\sigma_\lambda = \frac{2.8}{\gamma}\sqrt{\frac{2}{\pi}}\cdot\begin{cases}\left(\dfrac{\lambda}{10\lambda_c}\right)^{0.354} & \text{for } \lambda > 10\lambda_c \\ \left(\dfrac{\lambda}{10\lambda_c}\right)^{0.549} & \text{for } \lambda < 10\lambda_c\end{cases} = 2.8\sqrt{\frac{2}{\pi}}\cdot\begin{cases}\gamma^{0.062}\left(\dfrac{3}{40\pi}\dfrac{\lambda}{\rho}\right)^{0.354} & \text{for } \lambda > 10\lambda_c \\ \gamma^{0.647}\left(\dfrac{3}{40\pi}\dfrac{\lambda}{\rho}\right)^{0.549} & \text{for } \lambda < 10\lambda_c\end{cases} \quad (16)$$

If the wavelength is always chosen where the emission peaks, around the critical wavelength λ_c (Figure 2), then the width is indeed proportional to $1/\gamma$. But here we fix the wavelength in the visible while the critical wavelength changes during the ramp. Then for long wavelengths (upper expression), the width is almost independent of beam energy, while for short wavelengths (lower expression) it *increases* at nearly the 2/3 power of γ.

We will see below that a wide emission angle worsens blurring from depth of field. To get a narrower angle, we choose 400 nm, at the short end of the visible. At this wavelength, the lower expression for σ_λ pertains at all LHC energies for both protons and lead ions (Figure 1). Then the opening angle is proportional to $\gamma^{0.647}$, and depth-of-field blurring increases with energy. Moreover, since the beam's normalized emittance is maintained through the ramp, and since the beam size depends on the square root of the (unnormalized) emittance, the size we must measure is proportional to $\gamma^{-0.5}$. We will concentrate on the highest energy, 7 TeV, since it presents the most difficult case, but also include calculations for lower energies.

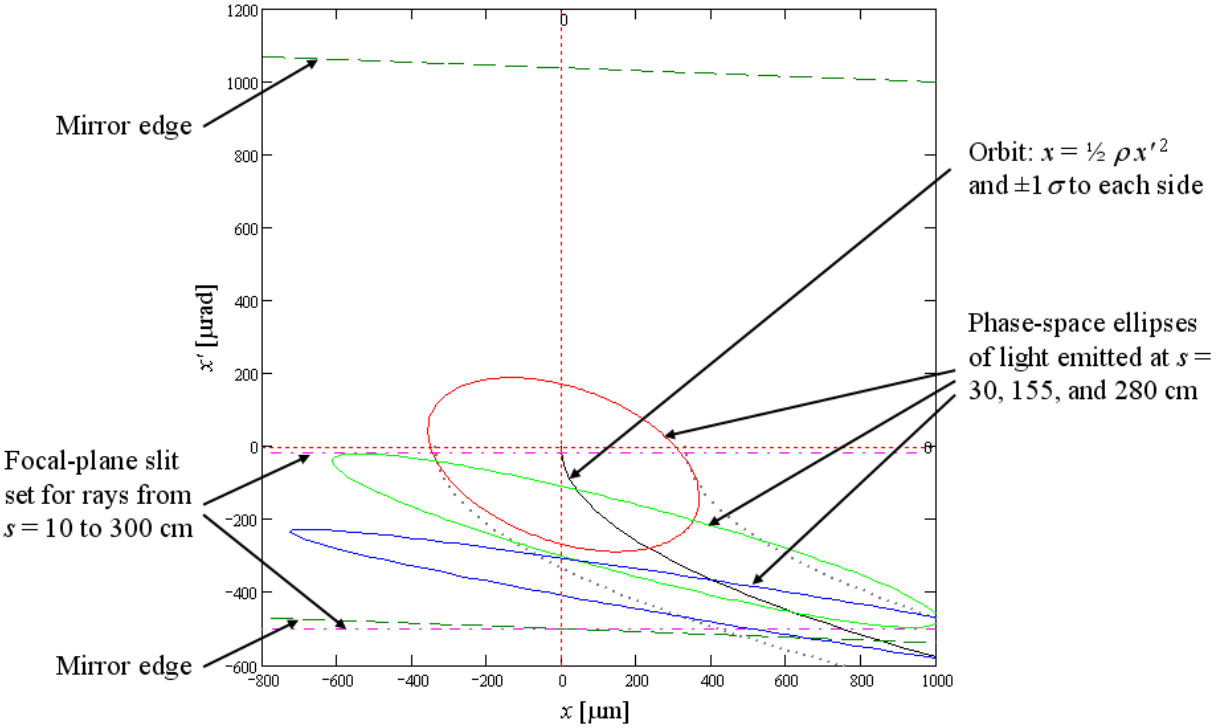

Figure 14. A repetition of Figure 13, but with phase-space ellipses of the light rays replacing the proton ellipses. The height of the ellipses is comparable to the slit spacing.

Protons at 7 TeV have an opening angle of 238 μrad for 400 nm (and nearly cross the boundary in Eq. (16)). Ions, with their smaller γ, have an angle of 131 μrad at the top of the ramp, making protons the more difficult case. (Diffraction, which favours larger angles, is discussed in Section 6.)

This angle is usually observed vertically, since dipole radiation forms a continuous horizontal stripe as the particle bends. However, this angle spread is also associated with the width of horizontal emission from every point along the orbit. Every proton in one of the ellipses along the orbit of Figure 13 emits light over a range of x angles with an RMS spread given by (16). The ellipse of the light at a point on the orbit s is a convolution of the ellipse of the protons at s and the much wider angular spread of the emission. The height of the light ellipse at s is dominated by the emission angle, while its width is that of the proton ellipse; consequently, the light ellipse at s is nearly aligned with the xx' axes.

To see how light emitted at a point s enters the image, we transport its ellipse through the drift space to the focal plane. Figure 14 is identical to Figure 13, except that the proton ellipses have been replaced by 1-sigma ellipses of light rays from the same points on the orbit. Because these ellipses are vertically wide and

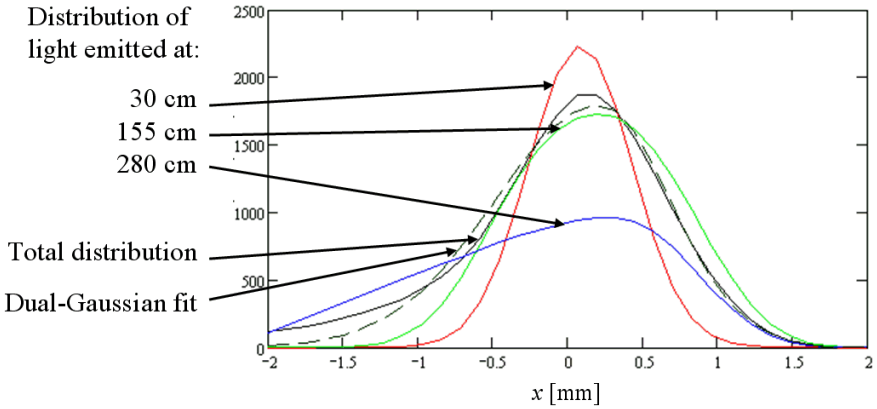

Figure 15. Projections of the light ellipses of Figure 14 onto the x axis. Since the ellipses shift progressively to the right but are increasingly cut by the slit, the total distribution is asymmetric with a long tail on the left.

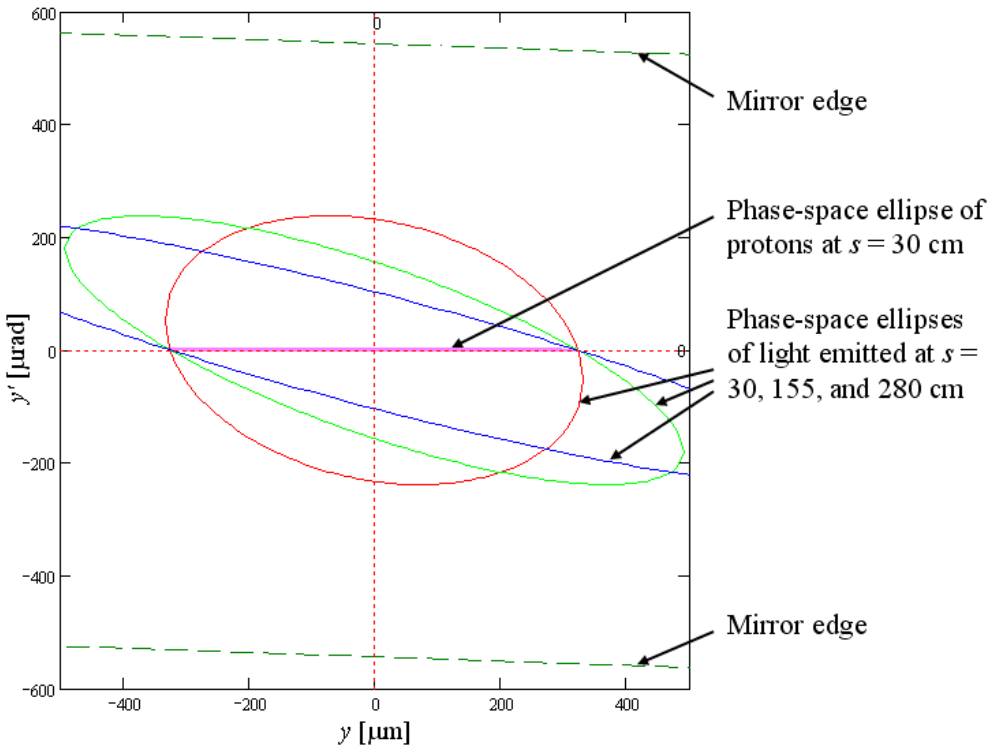

Figure 16. Vertical phase space of the protons and of their emitted dipole radiation, with the coordinates and the optical focus in the plane of the dipole entrance.

have been transported from three typical emission points inside the dipole to the focal plane at the dipole entrance, the tilt of each ellipse grows with the transport distance.

Only the ellipse from the middle of the path (s = 155 cm) is fully contained within the slit boundaries. But the slit cuts light even from this emission point, since the ellipses are drawn at their 1-sigma contours. Consequently, the slit does not precisely select a slice of the orbit inside the dipole that contributes to the image.

Figure 15 shows a projection of the light ellipses from every contributing portion of the path onto the x axis. The composite distribution is broadened by the long and tilted ellipses from points deep within the dipole. But the rightward shift from these points is limited by the more severe cutting of light on the right from points deep within the dipole (such as the 280-cm ellipse in Figure 14). The outcome is a long tail on the left, but a Gaussian-like drop on the right that is very close to the expected beam size. Thus we fit the distribution with two Gaussians, one on each side, meeting at their peaks with different widths. Points below 10% of the peak are not used in the fit, to avoid the long tail. On the left, the Gaussian is over twice the width of the beam, but on the right only 42% wider.

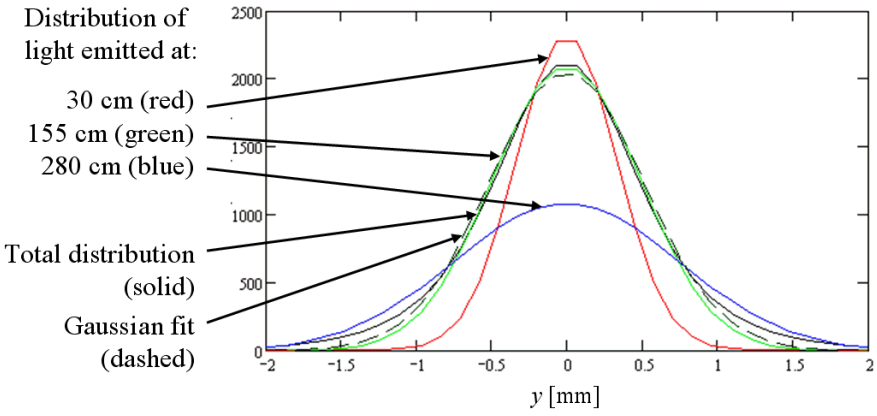

Figure 17. Beam ellipses of Figure 16, projected onto the y axis. The focus is at the dipole entrance, and there is significant broadening of the total distribution.

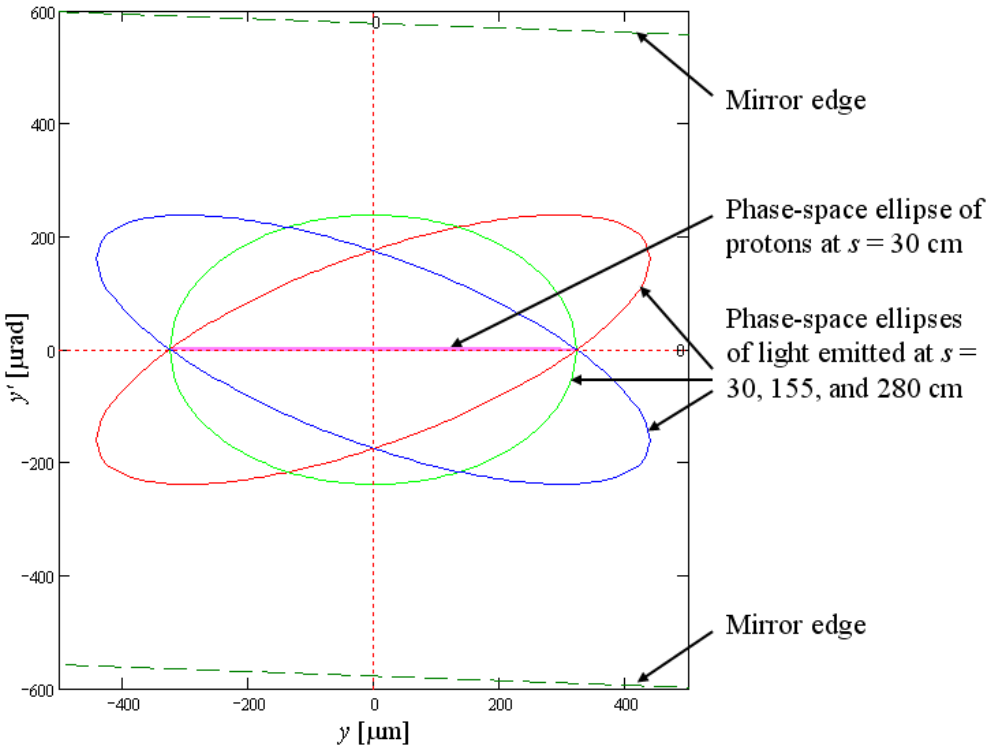

Figure 18. Vertical phase space. Like Figure 16, but with the origin and optical focus shifted to s = 155 cm.

(These sizes do not yet include diffraction.) Ways to improve on this outcome will be considered in Section 5.5, after looking at vertical phase space.

One helpful effect acts to limit broadening from depth of field: there is no dipole, and hence no dipole radiation, for $s < 0$. In fact the central radiation in our spectral band does not really start until $s \approx 10$ cm. At 7 TeV, we have seen that proton edge radiation is not distinct from central radiation, and the undulator radiation is negligible. The exclusion of contributions for $s < 10$ cm helps to reduce the tail of the total distribution in Figure 15.

5.4 Acceptance in *yy'* Phase Space

Figure 16 shows a similar plot of the vertical phase space, again for the case with the origin at the dipole entrance. Because the orbit has no vertical curvature, the light is emitted as a series of cones along a line. With the optics focused at the dipole entrance, images of points further inside the dipole are increasingly out of focus, forming wide projections on the y axis. Figure 17 shows these projections and the overall distribution from the same long path as in Figure 15. An RMS vertical size of 315 μm at the focal plane broadens by 57% to 496 μm (before including diffraction).

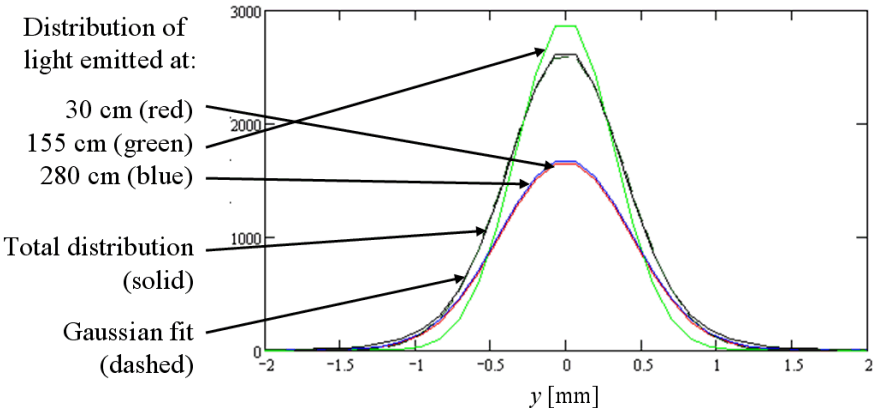

Figure 19. Beam ellipses of Figure 18, projected onto the y axis. The broadening is reduced by focusing at 155 cm, in the middle of the portion of the orbit from which the light is collected.

The horizontal slit still has an effect, since rays that lie in the vertical acceptance of

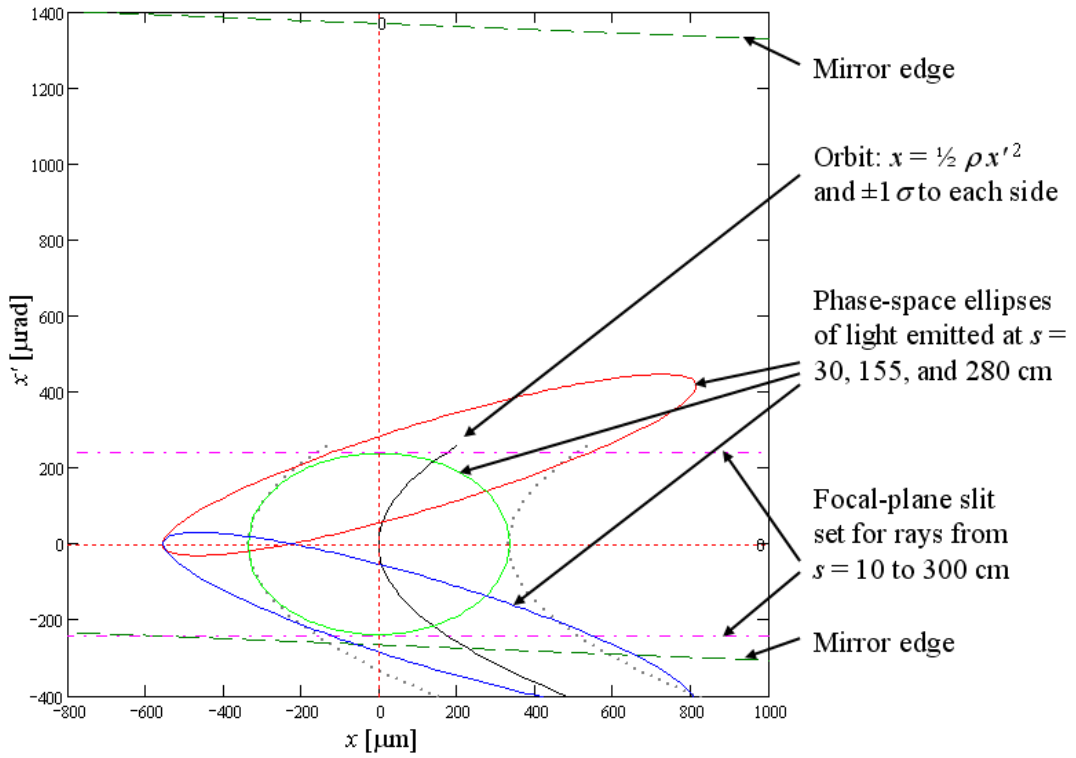

Figure 20. Horizontal phase space. Like Figure 14, but with the origin and optical focus shifted to s = 155 cm.

the mirror can still be blocked by their horizontal component. To find the total projections in Figure 15 and Figure 17, the full four-dimensional phase space for each emission point s was first cut by the horizontal slit and by the edges of the extraction mirror before projecting the remainder onto the x or y axis.

5.5 Focusing inside the Dipole

Much of the broadening of both the horizontal and vertical measurements comes from elongated ellipses emitted far from the focal plane. This observation suggests that the measured size could be reduced by shifting the focal plane from the dipole entrance to a point near the middle of the path over which light is collected.

Figure 18 shows another view of vertical phase space. The slit is again set to accept tangent rays emitted between s = 10 and 300 cm from the entrance, but now the origin and focus are shifted to s = 155 cm, the middle of this range. The ellipses are from the same points on the path as those in Figure 16, but the widest one is transported through half the distance and so is half as wide. Figure 19 shows the corresponding projections, which bear out these qualitative remarks. The width of the sum distribution is 384

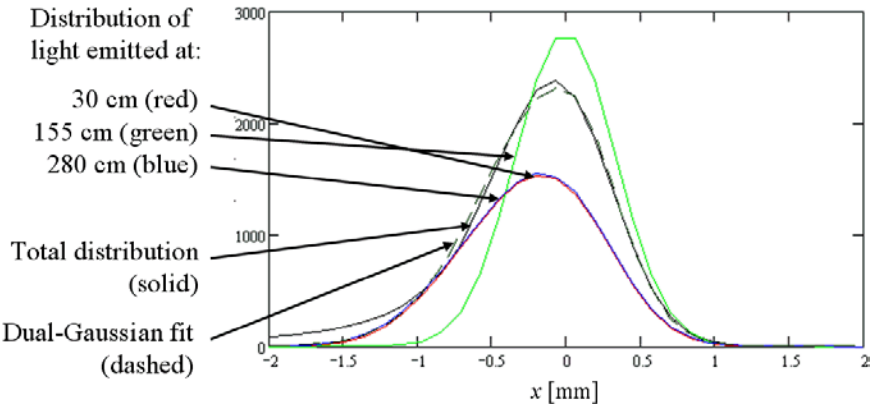

Figure 21. Beam ellipses of Figure 20, projected onto the x axis. As in the vertical, broadening is reduced by focusing at 155 cm, in the middle of the portion of the orbit selected by the slit.

μm, an increase of 22% (before diffraction), rather than the 57% found when focusing at the entrance.

Setting the slit for a shorter path can help somewhat to further reduce broadening, but this gain is limited by the wide ellipses: some light from points beyond the slit's nominal cut-off still enters into the distribution. Because of this effect, a small additional improvement can be found in moving the focus from the exact centre of the path toward the downstream end, since the reduction in broadening from these interior points is not offset by upstream points: as noted earlier, there is no contribution from $s < 10$ cm, as the field rolls off. Table 1 lists some examples of shifting the focus in this way.

Adding a vertical slit can help a bit to further define the region from which light is collected, but the mirror's vertical edge effectively plays that role now. Recall that the ellipses in Figure 18 are 1-sigma contours, and so the mirror cuts just above the 2-sigma point, even for light from the middle of the region of interest. A significantly narrower slit would cut desired light and also add to diffraction.

In the horizontal plane, shifting the focus to the middle of the path is also quite helpful. Horizontal phase space is plotted in Figure 20, and Figure 21 shows the distributions on the x axis. The overall distribution gives an improved width measurement of 350 μm, only 4.6% over the correct size at the focal plane (using the Gaussian fit to the right side, before diffraction).

Table 1 lists the detailed results for protons and ions, including the effects of depth of field and diffraction (taken from the following section). The entries in red italics show the effect of varying the slit width at constant beam energy. Measurements using light from the dipole centre are more sensitive in the vertical plane to depth of field than in the horizontal. Both horizontal and vertical measurements (considering for now only depth of field) grow similarly as the slit widens, but the wide ellipses at 7 TeV reduce the sensitivity to slit width.

The entries with yellow shading show how the expected size measurements vary with beam energy. Undulator radiation is used at low energies, without depth of field (see Section 6.3). Two intermediate energies are listed: 1.5 and 3.5 TeV (or equivalent). The first is where the signal is low for both protons and ions, since the visible emission from the undulator has dropped off, but the light from dipole is still weak. The second is the energy chosen for the first collision run. Depth of field does not broaden the measurements significantly at 3.5 TeV and below, because the ellipses are narrow. Horizontally, the balance between rightward stretching of the sum distribution and cutting on that side by the slit (discussed in Section 5.3) causes the depth of field effect to *decrease* with energy, but the effect on the fitted width is small throughout.

For protons at collision energy, a path of 2 m, focused at $s = 125$ cm (slightly past the midpoint) offers a reasonable compromise between light collection and resolution in both planes; the table shows this choice in boldface. With this setting, the horizontal size at 7 TeV is determined correctly, but the vertical size is overestimated by 17%. Lead ions, which are less affected by depth of field due to their lower γ, can use a 3-m path. Since there is sufficient light from a 2-m path at 7 TeV equivalent, this distance is used (with the focus at the midpoint) for both protons and ions in the diffraction calculations of Section 6.1 and the signal calculations of Section 7.3.

Table 1. Calculated beam size versus energy and slit setting. Undulator calculations use wavelength near peak; other cases use 400 nm. The colours are explained in the text.

Beam Energy	Wave-length	Slit Setting (Range in Dipole) and Focus Position			Beam Size at Source		Angle Span Accepted by Slit	At Camera (Magnification=0.3)		
					Proton Beam	With Depth of Field		Diffraction Resolution	Calculated Size Measurement	
TeV (equiv)	*nm*	Start *cm*	Focus *cm*	End *cm*	*μm RMS*	*μm RMS*	*μrad RMS*	*μm RMS*	*μm RMS*	*Ratio to True Size*
Protons: Horizontal										
0.45	609	Centre of Undulator			1301.5	1301.5	492.2	107.6	391.2	1.002
1.5	400	10	105	200	721.8	725.7	112.3	136.3	218.1	1.007
3.5	400	10	105	200	472.6	485.8	113.2	111.1	146.0	1.030
5	400	10	105	200	395.3	402.7	114.3	100.7	121.0	1.021
7	*400*	*10*	*55*	*100*	*333.3*	*321.4*	*58.9*	*162.4*	*162.4*	*1.624*
7	*400*	*10*	*80*	*150*	*333.7*	*321.8*	*87.2*	*109.7*	*109.7*	*1.096*
7	*400*	*10*	*105*	*200*	*334.0*	*327.6*	*115.5*	*90.3*	*98.5*	*0.983*
7	**400**	**10**	**125**	**200**	**334.3**	**334.8**	**115.5**	**91.3**	**100.7**	**1.004**
7	400	10	150	200	334.6	342.2	115.5	92.3	102.9	1.025
7	*400*	*10*	*130*	*250*	*334.4*	*334.6*	*144.5*	*81.6*	*100.6*	*1.003*
7	400	10	0	300	332.6	472.7	171.0	89.2	142.1	1.424
7	*400*	*10*	*155*	*300*	*334.7*	*350.1*	*172.3*	*76.5*	*105.2*	*1.048*
7	400	10	180	300	335.1	355.2	172.2	77.0	106.8	1.062
7	400	Dipole Edge			332.6	332.6	37.0	258.9	258.9	2.595
Protons: Vertical										
0.45	609	Centre of Undulator			1244.1	1244.1	619.1	93.5	372.7	0.999
1.5	400	10	105	200	681.3	683.8	88.0	148.9	204.8	1.002
3.5	400	10	105	200	446.6	463.0	152.2	93.2	138.7	1.035
5	400	10	105	200	373.0	406.9	191.6	77.9	121.9	1.089
7	*400*	*10*	*55*	*100*	*315.1*	*369.1*	*236.5*	*66.8*	*110.6*	*1.170*
7	*400*	*10*	*80*	*150*	*314.9*	*369.0*	*236.6*	*65.1*	*107.9*	*1.142*
7	*400*	*10*	*105*	*200*	*314.8*	*371.6*	*236.7*	*67.0*	*111.4*	*1.179*
7	**400**	**10**	**125**	**200**	**314.7**	**368.4**	**236.6**	**66.7**	**110.4**	**1.169**
7	400	10	150	200	314.6	368.1	236.6	66.7	110.3	1.169
7	*400*	*10*	*130*	*250*	*314.7*	*378.7*	*236.7*	*67.6*	*113.5*	*1.202*
7	400	10	0	300	315.4	495.8	236.0	77.5	148.5	1.570
7	*400*	*10*	*155*	*300*	*314.6*	*383.8*	*236.8*	*68.1*	*115.0*	*1.219*
7	400	10	180	300	314.4	383.1	236.8	68.0	114.8	1.217
7	400	Dipole Edge			315.4	315.4	59.6	159.9	159.9	1.690
Lead Ions: Horizontal										
0.45	800	Centre of Undulator			1303.7	1303.7	1317.0	75.5	392.2	1.003
1.5	400	Centre of Undulator			714.1	714.1	459.9	68.1	218.7	1.021
3.5	400	10	105	200	473.4	478.5	112.5	110.6	143.8	1.013
5	400	10	105	200	396.0	404.5	112.3	101.8	121.6	1.024
7	*400*	*10*	*105*	*200*	*334.6*	*345.0*	*112.6*	*93.9*	*103.7*	*1.033*
7	*400*	*10*	*130*	*250*	*334.9*	*348.9*	*141.4*	*84.2*	*104.9*	*1.044*
7	*400*	*10*	*155*	*300*	*335.3*	*355.3*	*171.5*	*77.2*	*106.8*	*1.062*
7	400	Dipole Edge			333.1	333.1	90.6	105.6	105.6	1.056
Lead Ions: Vertical										
0.45	800	Centre of Undulator			1246.2	1246.2	2192.6	57.3	375.2	1.004
1.5	400	Centre of Undulator			683.6	683.6	607.3	60.4	218.0	1.063
3.5	400	10	105	200	447.4	450.7	84.0	123.8	135.0	1.006
5	400	10	105	200	373.6	380.7	105.7	101.4	114.0	1.017
7	*400*	*10*	*105*	*200*	*315.4*	*329.8*	*131.4*	*84.6*	*98.8*	*1.044*
7	*400*	*10*	*130*	*250*	*315.2*	*333.2*	*131.4*	*85.1*	*99.8*	*1.055*
7	*400*	*10*	*155*	*300*	*315.1*	*337.1*	*131.4*	*85.6*	*101.0*	*1.068*
7	400	Dipole Edge			315.9	315.9	146.0	78.6	94.6	0.998

6 Diffraction

For a given angular spread, the smallest optical waist, and hence the best size resolution, is given by the TEM_{00} (Gaussian) mode. This sets a lower bound on the resolvable beam size. For a given wavelength λ, the mode's RMS transverse size σ_r and angle spread σ_λ obey:

$$\sigma_r \sigma_\lambda = \frac{\lambda}{4\pi} \tag{17}$$

A TEM_{00} beam at λ = 400 nm with a 330-μm-RMS waist has a 100-μrad-RMS angle spread.

6.1 Diffraction of Radiation from the Dipole Centre

Equation (17) argues for a short wavelength and a wide angle spread. However, the two are linked. For central dipole radiation, Eq. (16) shows that the angle spread is proportional to either $\gamma^{0.062}\lambda^{0.354}$ or $\gamma^{0.647}\lambda^{0.549}$, with the second case applying for our range of critical wavelengths. The resolvable size then is proportional to $\gamma^{-0.647}\lambda^{0.451}$. As in Section 5.3, we are led to the choice of 400 nm. Unlike depth-of-field blurring, the diffraction resolution improves as the energy increases, at least until the critical wavelength crosses the boundary in (16). Once $\lambda >> \lambda_c$, the resolution is proportional to $\gamma^{-0.062}\lambda^{0.646}$, again preferring short wavelengths but with no significant energy dependence.

As was noted in Section 5.3, the beam size, and so the required resolution, is proportional to $\gamma^{-0.5}$. Consequently, for central dipole radiation at wavelengths $\lambda << \lambda_c$, the ratio of beam size to diffraction resolution is proportional to $\gamma^{0.147}$, a weak improvement with energy (and proportional to $\gamma^{-0.438}$ for $\lambda >> \lambda_c$). Since depth of field is more difficult at 7 TeV, we emphasize the effect of diffraction on dipole central and edge radiation at this energy, but also consider the full energy range. We then combine all sources of broadening.

The calculations use the physical-optics mode of ZEMAX, which models the propagation through the full optical system of a monochromatic Gaussian beam (set here to 400 nm) with different horizontal and vertical divergence angles. The result combines the geometric-optics blurring shown in Figure 11 with diffraction to find the size of the Gaussian image on the camera. (Note that the software uses the common definition of the size as the intensity's half width to e^{-2}, usually called ω, rather than its RMS width σ; these are related by $\sigma = \omega/2$. A similar definition applies to the divergence.) The calculation gives a lower bound on the resolution of the actual source beam, and can also be scaled for a non-Gaussian source beam, as discussed below.

Diffractive broadening depends on the angular distributions, which are calculated as projections of the horizontal (Figure 20) and vertical (Figure 18) phase space onto the x' and y' axes, as shown in Figure 22. Vertically the distribution is nearly Gaussian and remains constant with path length. Horizontally, the angle distribution is set by the slits, but with complications. The slit cuts the light at fixed angles, making a sharp rise and fall. One side of the slit is fixed in all cases studied, cutting at the point intercepted by tangent rays from the orbit at s = 10 cm. As the other side moves, the focal point is also shifted, usually to the centre of the selected path. As we have seen, the slit passes portions of the light ellipse from points beyond its nominal selection, but there is no light from points beyond the edge of the dipole at s = 0. Consequently, the distribution in horizontal angle is not uniform, as in Figure 5(a), but droops as x' increases. The rounding of the peak in Figure 22(a) arises because the mirror's edge rather than the slit becomes the limit for $x < -600$ μm (see Figure 20). We fit a Gaussian to the projections of Figure 22 to provide input for the ZEMAX calculation.

The ZEMAX computation of the image size on the camera requires an appropriate Gaussian to model the source, which does not in general fit a TEM_{00} transverse mode. The source's size (broadened by depth of field) is given by the Gaussian fits of Figure 19 and Figure 21, and its angular divergence is given by the fits of Figure 22. The product of the source width and opening angle could be either larger or smaller than that given for light in Eq. (17): to pick an extreme case, the source could (in principle) be as small as a single proton.

For the simplest case, in which the size-angle product of a particle beam matches (17), the resolution of a beam measurement should be the same as that obtained with TEM_{00} light. If the product is smaller (as in the case of that single proton), then the beam's image is restricted to a resolvable spot no smaller than that of the optical mode.

If the size-angle product of an optical waist is larger than (17), then it may be regarded as a mixture of transverse (laser) modes [8]. Such an optical beam is commonly characterized by a parameter called M^2, given by:

$$\sigma_r \sigma_\lambda = M^2 \frac{\lambda}{4\pi} \tag{18}$$

In general, $M^2 \geq 1$, with the equality applying to the TEM_{00} mode. (This relationship is again more conveniently expressed using the product of the e^{-2} sizes rather than the RMS values used here.) Siegman [9] showed that a mode mixture propagates by tracking an "embedded" TEM_{00} mode. Both the beam's radius and divergence angle are wider than those of the embedded mode by a factor of M. The Rayleigh length remains that of the embedded Gaussian, and the value of M^2 is conserved.

Thus when the equivalent M for the emission from the particle beam is greater than 1, we use M to find the embedded mode and to scale the image size found by ZEMAX. When $M < 1$, we propagate an embedded Gaussian in ZEMAX with a divergence equal to that of the light emitted by the particle beam. The calculated image size is taken to be the size of the image of the particle beam.

Table 1 lists the results of these resolution calculations. In addition to the blurring from geometric imaging, depth of field, and diffraction discussed

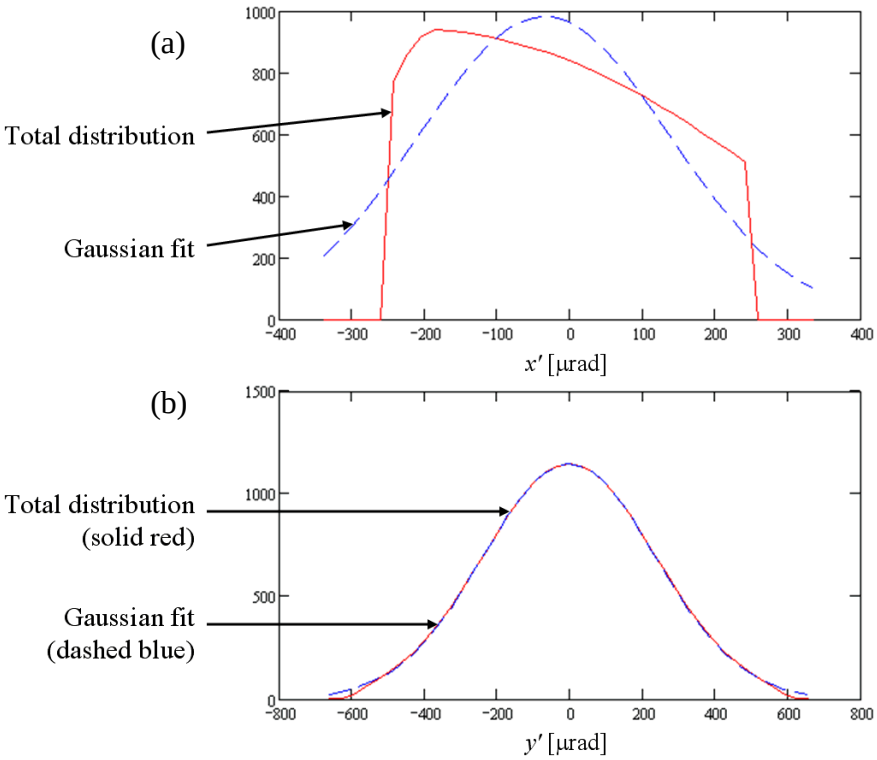

Figure 22. (a) Horizontal and (b) vertical angular distribution of light, including cuts by the slit and mirror edges. The distribution are projections of the phase space (Figure 20 and Figure 18 respectively) onto the x' and y' axes.

previously, the rightmost columns show the diffraction resolution and the size of the beam's image from all effects. Vertically, as the path in the dipole selected by the slits increases, the diffraction resolution remains constant. Depth-of-field blurring increases, although the effect is gradual since (as noted above) the slits do not provide a hard edge in *s*. Horizontally, the angular width increases with path length; the decrease in diffraction balances the effect of depth of field. As noted before, a path of 2 m provides a good compromise between light collection and resolution in both planes. This path (with the focus at the midpoint) is used below to calculate the signal levels in Sections 7.3, 8.3, and 8.4.

6.2 Diffraction of Radiation from the Dipole Edge

Table 1 also lists the diffractive broadening of the edge radiation shown in Figure 5(b). Since the profile is approximately Gaussian in both planes, the RMS value of the angular emission pattern at 400 nm provides the input for the calculation. We see that diffraction more than doubles the measured size of a 7-TeV proton beam. As discussed earlier, the expression (6) for edge radiation is beyond its region of validity for this case. For lead ions at 7 TeV equivalent, the expression remains valid, and their lower γ gives horizontal and vertical emission angles that are wide enough to avoid diffractive broadening.

6.3 Depth of Field and Diffraction of Undulator Radiation

The undulator is used at low γ, where the emission angle is wide, as Figure 6(c) shows. Its 56-cm length is sufficient to ask how depth of field might affect the image. However, the emission pattern given by Eq. (10) is not a local property of each short segment of the undulator, to be combined as was done for dipole radiation. Rather the equation incorporates the interference of light emitted along the full length of the undulator, and so we place the focus in the middle of the undulator.

In the discussion of central dipole radiation above, a constant measurement wavelength of 400 nm was found to be best. But Eq. (9) shows that the undulator emission peaks on axis at a wavelength of $\lambda_u/(2\gamma^2)$. Longer wavelengths are emitted in rings at increasing angles from the axis. The minimum opening angle is then found at the peak, where the RMS emission angles along the horizontal and vertical axes, normalized to $1/\gamma$, are:

$$\begin{aligned} \sigma_\xi &= 0.236 \\ \sigma_\psi &= 0.299 \end{aligned} \tag{19}$$

These normalized angular widths are independent of beam energy. Without normalization, 450-GeV protons have RMS angles of 492 and 619 μrad at the 608-nm peak wavelength. Even at this long wavelength, these wide angles mean that diffraction is not a concern (Table 1), and it is not an issue across the energy range in which undulator radiation will be used.

For lead ions at injection, the undulator's peak wavelength is 3.8 μm, too far into the infrared for our video cameras (see Section 7.2). Table 1 evaluates the image size at 800 nm, the longest wavelength with reasonable response from the camera. The table also lists a case with ions at 1.5-TeV equivalent. The undulator is still the dominant source, but the peak wavelength is now 345 nm, and so we evaluate the size at 400 nm, the standard wavelength used in the rest of the table.

7 Camera Signals

7.1 Photons Arriving at the Camera

Section 3 found the energy per particle emitted by the three sources. Figure 10 showed that the spectrum arriving at the camera is modified by the transmission of the window and the reflectivity of the mirrors. For protons, the strongest effect is the cut-off of the ultraviolet by the protected silver mirrors. The spectrum of lead ions is largely infrared at injection, but the window (Figure 10(a)) removes wavelengths longer than 4 μm and also leaves a gap near 2.8 μm. These effects are included here to find the photon count at the camera.

Table 2. Proton and lead-ion fills. For ions, a pilot bunch is the same as a nominal bunch.

	Protons	**Pb Ions**
Particles in a pilot bunch	5×10^{9}	7×10^{7}
Particles in a nominal bunch	1.15×10^{11}	7×10^{7}
Bunches in an early fill	43	62
Bunches in a full ring	2808	592

Figure 23(a) shows the resulting count of photons per proton per turn arriving at the camera. (The camera's response will be considered next.) The curve for the dipole's central radiation uses a path extending to 2 m inside the dipole, as discussed in Sections 5.5 and 6.1. Scaling the plotted values by the number of protons in the machine, from Table 2, gives the total number of photons arriving at the camera. At injection, a single pilot bunch of 5×10^{9} protons sends 5.4×10^{4} photons from the undulator to the camera in one turn. At 1 TeV, this value drops to 1.1×10^{4} (summing edge and central dipole radiation) and then recovers strongly to provide 1.9×10^{7} photons from the dipole centre at 7 TeV.

Figure 23(b) shows a similar plot for lead ions. The large charge per ion greatly increases the light produced per particle. The change in the relative output of the three sources is due to the matching of their emission spectra with the pass-band of the optics. The undulator's peak (Figure 3) passes from infrared at injection

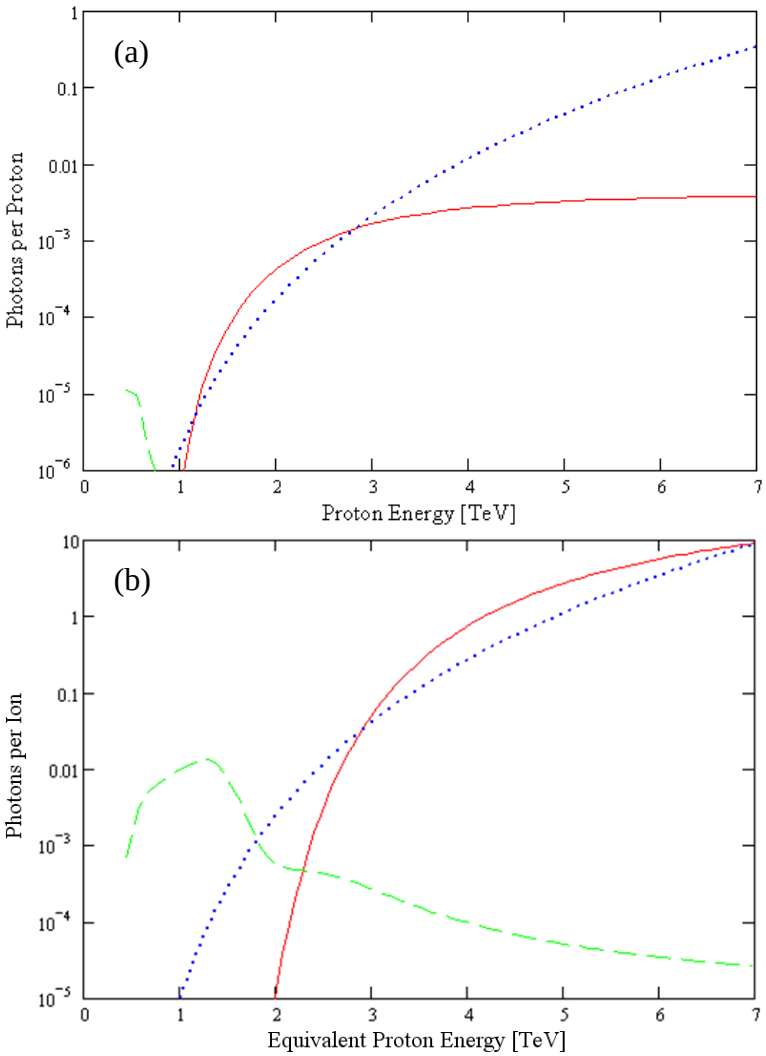

Figure 23. Photons per turn per (a) proton and (b) lead ion, arriving at the camera as a function of the (equivalent) proton energy. The source is the dipole centre (solid red), the dipole edge (dotted blue), and the undulator (dashed green), for wavelengths between 380 and the infrared cut-off of the fused-silica viewport.

into the visible around 1 TeV (equivalent), leading to the peak in the plot. A single injected bunch of 7×10^7 ions sends 4.9×10^4 photons per turn to the camera. At collision energy, this rises to 1.2×10^9.

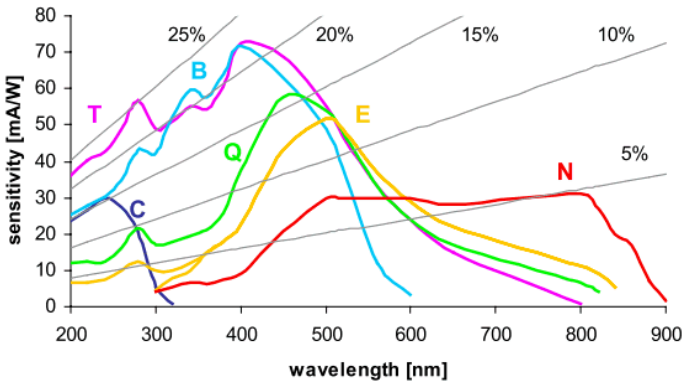

Figure 24. Spectral response of the Proxicam intensified camera, which has a photocathode following curve N.

7.2 Camera Properties

Two cameras will be used to measure beam profiles. One, a Proxicam type HL4 S NIR with a red-enhanced S25 photocathode (the "Proxicam"), has a built-in image intensifier, which will be useful at lower beam energies. However, it has no fast gating or framing capability, and so is not suitable for bunch-by-bunch or rapid turn-by-turn imaging. Its spectral response is shown in Figure 24. Since it will be the main camera for profiling the beam using light from all bunches over multiple turns, it is the basis for the calculations that follow. The image area on the photocathode is 12.8 mm by 9.6 mm. The intensifier output is fibre-coupled with an 18:11 reducing taper to the CCD, which has 756 by 581 pixels. Imaged back to the cathode, the pixels are almost square, 16.9 μm by 16.5 μm.

The second camera, a Redlake MotionXtra HG-100K E (the "Redlake"), has a fast-framing capability suitable for turn-by-turn images. At full resolution, it can take 1000 frames/s, or 10,000 frames/s using a 352×352-pixel region. It can store 1264 full frames, and correspondingly more of the lower-resolution frames, until readout after an acquisition sequence. It has no built-in intensifier, and so cannot select a single bunch. However, an external intensifier with gating capability has been mounted on the camera, using a lens to couple the light from the intensifier's phosphor screen to the camera's photocathode. Lens coupling is inherently inefficient, gathering only a small solid angle, and so the intensifier now provides only a small intensity gain, at best. Future plans call for buying a fibre-coupling assembly for the Redlake so that it can record bunch-by-bunch and turn-by-turn beam images.

7.3 Photoelectrons

Figure 25 shows the number of photoelectrons per particle produced at the photocathode of the Proxicam, as a function of beam energy. The insertable beamsplitter that shares the light with the Redlake is assumed to be out, since that camera is intended for occasional studies. We integrate over the spectrum of each source, modified by both the pass-band of the optics and the camera's response. The full energy range can be divided into three zones. Each draws light from a different source or mixture of sources, as their relative power changes and as the slit on the focal plane of F1 is adjusted to enhance the exclusion of unwanted sources, as discussed below:

Zone 1: Low Energy
- Protons: 0.45–1.25 TeV.
- Lead ions: 0.45–2.6 TeV (equivalent).
- Light from the undulator only.
- The slit is wide to accept all angles reaching the extraction mirror.

Zone 2: Crossover
- Protons: 1.25–3 TeV.

- Lead ions: 2.6–7 TeV (equivalent).
- Light from both dipole central and edge radiation.
- The slit edge selecting the downstream end of the path in the dipole is set to take light from first 2 m.
- At the low end of this zone, the upstream slit edge is set to take a comparable angular width to that taken by the downstream side, because the edge radiation is still wide. This slit jaw then narrows with energy in order to reduce the contribution of edge radiation at the start of the third zone.

Zone 3: High Energy

- Protons: 3 – 7 TeV.
- Lead ions: Not needed, since this zone would start above 7 TeV equivalent.
- Light from dipole central radiation only.
- The downstream slit edge is still set for light from first 2 m of path in the dipole.
- The upstream slit edge is set to accept tangent rays from 10 cm or more inside the dipole.

The boundary between zones 2 and 3 lies at the onset of the problems previously identified with edge radiation. Since Eq. (6) is valid only when $\lambda << \lambda_c$, and since the longest wavelength detected by the camera is 900 nm, we set the boundary where λ_c = 900nm, which falls at 2.8 TeV for protons and 7.1 TeV equivalent for ions. It is difficult to exclude edge radiation entirely without cutting central radiation. In the end, these adjustments will be made empirically.

Good measurements are difficult at the exact crossover. Until the undulator light drops an order of magnitude below the dipole light, it enters the camera as a significant out-of-focus source. The effect of the linear adjustment of the slit width in the crossover zone can be seen in Figure 25 in the fast decline of the undulator component for protons above 1.25 TeV and for ions above 2.6 TeV, and in the notch in proton edge radiation at the 3-TeV zone boundary. The cleanest solution is to turn the undulator off at this stage in the ramp. For a conservative estimate of the signal on the

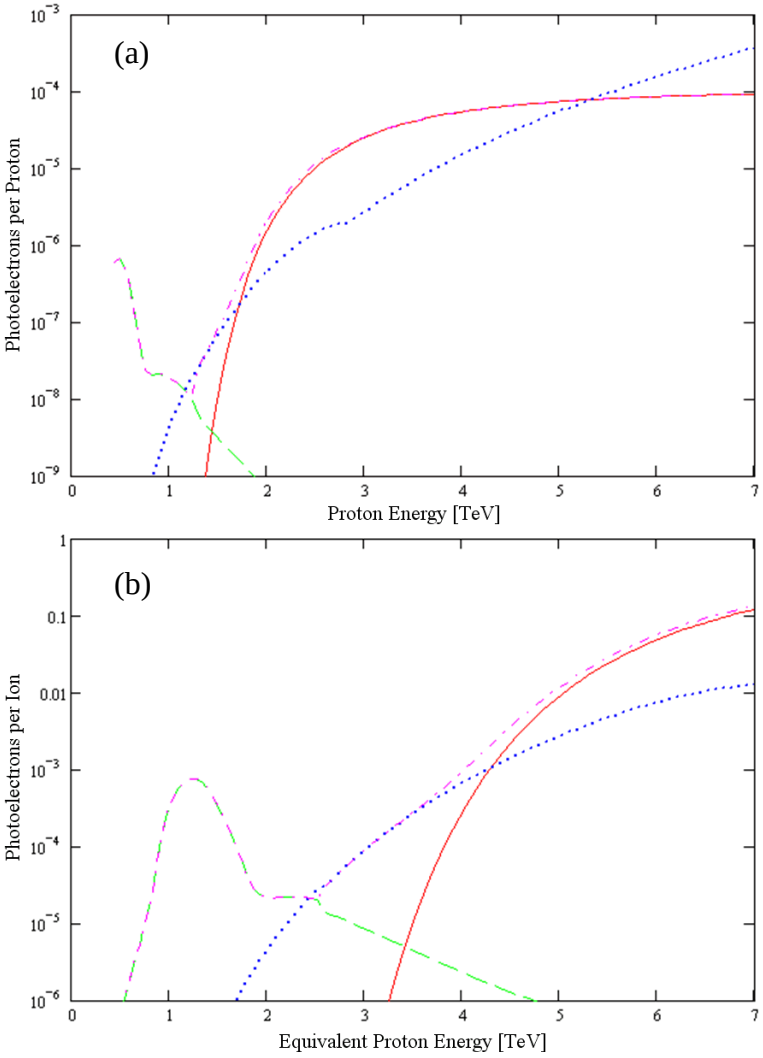

Figure 25. Photoelectrons (a) per proton, and (b) per lead ion, at the photocathode of the Proxicam, for light from the dipole centre (solid red), the dipole edge (dotted blue), and the undulator (dashed green). The fourth curve (dash-dot magenta) represents the selection made at each energy by the source intensity and by the slit.

Table 3. Photoelectrons at the Proxicam's photocathode, total and in the peak pixel, for various beam energies and for the fill patterns of Table 2. The beamsplitter sending light to the Redlake is out. The size of the image on the camera, used to find the signal in the peak pixel, is taken from Table 1, with the focus centred between slit settings of 10 and 200 cm. The "best resolution" case uses only wavelengths from 500 nm to the window's cut-off. The dark current per pixel is also shown. The error in fitting to the *x* and *y* projections is due to noise and to the fit to a pixellated image.

	Protons				**Lead Ions**			
Energy [TeV]	**0.45**	**1.5**	**3.5**	**7**	**0.45**	**1.5**	**3.5**	**7**
Image Size								
σ_x [μm RMS]	391.2	218.1	146.0	98.5	392.2	218.7	143.8	103.7
σ_y [μm RMS]	372.7	204.8	138.7	111.4	375.2	218.0	135.0	98.8
σ_x [pixels RMS]	23.1	12.9	8.6	5.8	23.2	12.9	8.5	6.1
σ_y [pixels RMS]	22.6	12.4	8.4	6.7	22.7	13.2	8.2	6.0
Photoelectrons from a Pilot Bunch								
All pixels, 1 turn	2930	377	2.01×10^{5}	4.63×10^{5}	20.5	25100	18900	9.30×10^{6}
Peak pixel, 1 turn	0.893	0.376	442	1880	0.00621	23.5	43.4	40400
Peak pixel, 20 ms	201	84.6	9.94×10^{4}	4.22×10^{5}	1.40	5280	9750	9.09×10^{6}
Photoelectrons from a Nominal Bunch								
All pixels, 1 turn	6.44×10^{4}	8300	4.42×10^{6}	1.02×10^{7}	20.5	25100	18900	9.30×10^{6}
Peak pixel, 1 turn	19.7	8.28	9720	4.13×10^{4}	0.00621	23.5	43.4	40400
Peak pixel, 20 ms	4420	1860	2.19×10^{6}	9.29×10^{6}	1.40	5280	9750	9.09×10^{6}
Photoelectrons from an Early Fill								
All pixels, 1 turn	2.77×10^{6}	3.57×10^{5}	1.90×10^{8}	4.38×10^{8}	1270	1.56×10^{6}	1.17×10^{6}	5.77×10^{8}
Peak pixel, 1 turn	845	356	4.18×10^{5}	1.78×10^{6}	0.385	1460	2690	2.51×10^{6}
Peak pixel, 20 ms	1.90×10^{5}	8.00×10^{4}	9.40×10^{7}	3.99×10^{8}	86.6	3.27×10^{5}	6.05×10^{5}	5.64×10^{8}
Photoelectrons from a Full Ring								
All pixels, 1 turn	1.81×10^{8}	2.33×10^{7}	1.24×10^{10}	2.86×10^{10}	12100	1.49×10^{7}	1.12×10^{7}	5.51×10^{9}
Peak pixel, 1 turn	5.52×10^{4}	2.32×10^{4}	2.73×10^{7}	1.16×10^{8}	3.68	13900	25700	2.39×10^{7}
Peak pixel, 20 ms	1.24×10^{7}	5.23×10^{6}	6.14×10^{9}	2.61×10^{10}	827	3.13×10^{6}	5.77×10^{6}	5.38×10^{9}
Peak pixel, 20 ms, best resolution			1.50×10^{9}	7.75×10^{9}				9.37×10^{8}
Error in Beam Width from Fitting Projections for a Pilot Bunch with 20-ms Integration								
x width [%]	0.14	0.39	0.06	0.07	1.65	0.06	0.08	0.08
y width [%]	0.14	0.37	0.06	0.07	1.61	0.06	0.08	0.08
Dark Current								
Per pixel, 1 turn	7.46×10^{-6}				7.46×10^{-6}			
Per pixel, 20 ms	1.68×10^{-3}				1.68×10^{-3}			

camera, no undulator light is included for zones 2 and 3.

Scaling the photoelectrons by the number of particles in various fills (from Table 2) gives the number of photoelectrons collected, shown in Table 3. The table also lists the photoelectrons in the peak pixel, assuming a Gaussian beam image with the sizes given in Table 1. The calculations include photoelectrons emitted by protons and lead ions at four energies, in one turn and in one 20-ms video-integration interval. (The camera also can integrate over multiple video intervals.) The signal on the peak pixel varies strongly with energy (Figure 26), since the light level grows as the beam size shrinks.

The discussion of depth of field and diffraction showed that short wavelengths improve resolution with dipole radiation. Consequently, Table 1 used monochromatic light at 400 nm. More realistically, Table 3 includes a "best resolution" case that restricts wavelengths to the range from 380 nm (the mirror cut-off) to 500 nm. This is calculated only for central dipole radiation at 7 TeV (or equivalent), since this energy involves some broadening and has a large enough signal to permit wavelength selectivity.

Pixellation and noise can affect the measured image size. Eq. (114) of Ref. [1] gives an upper bound on the error $\Delta\sigma$ introduced by finding the RMS size σ of the x or y projection of an image recorded on pixels of width p:

$$\frac{\Delta\sigma}{\sigma} \le \frac{p^2}{8\sigma^2} \qquad (20)$$

Table 3 gives the expected RMS image widths. The bound from (20) ranges from 0.02% for a 23.2-pixel beam width to 0.35% for 6 pixels.

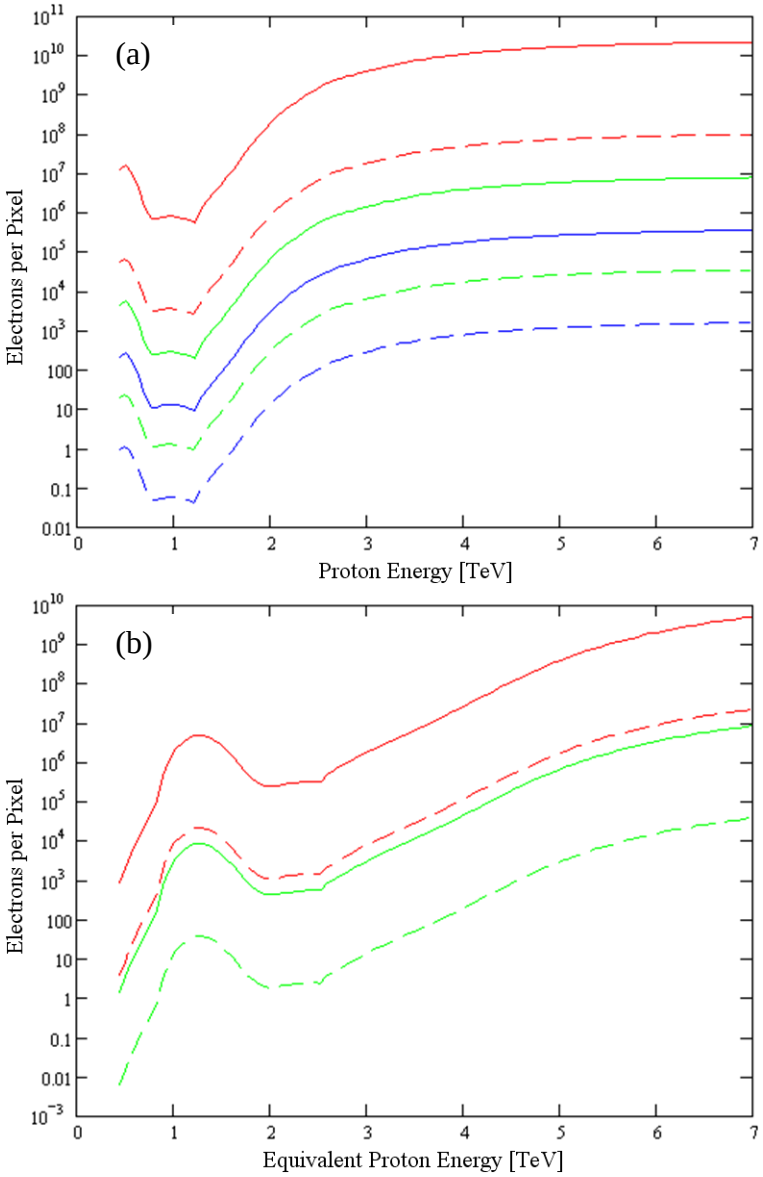

Figure 26. Electrons in the peak pixel of the Proxicam in one turn (dashed curves) and in a 20-ms interval (solid curves); for a pilot bunch (blue), a single nominal bunch (green), and a full ring (red). (a) Protons and (b) lead ions.

The actual errors, also in Table 3, are smaller, except at low energies where three noise sources increase $\Delta\sigma$. For weak signals, the dominant contribution is shot noise, which follows a Poisson distribution with the mean given by the expected number of photoelectrons per pixel at the cathode in an integration time, and the standard deviation by the square root of this number. Next, the Proxicam's intensifier and electronics are specified to have a signal-to-noise ratio of 36 dB (a factor of 63 in voltage). This Gaussian-distributed source exceeds shot noise for photoelectron counts over 4000. The photocathode's dark current (Table 3) adds more Poisson-distributed noise, but its rate of only 300 electrons·mm^{-2}·s^{-1} makes it negligible.

The effect of noise and pixellation was evaluated with a numerical model that calculates the signal on the camera pixels over the standard 20-ms video integration time (224 LHC turns). The Gaussian proton and ion beams of Table 3, including all three noise sources, were simulated. Then each x or y projection—sums of columns or rows of pixels—was fitted to a Gaussian of arbitrary height, width, mean and pedestal. For greater accuracy, the fitting function was also the integral of the Gaussian over the simulated pixels, summed to form a

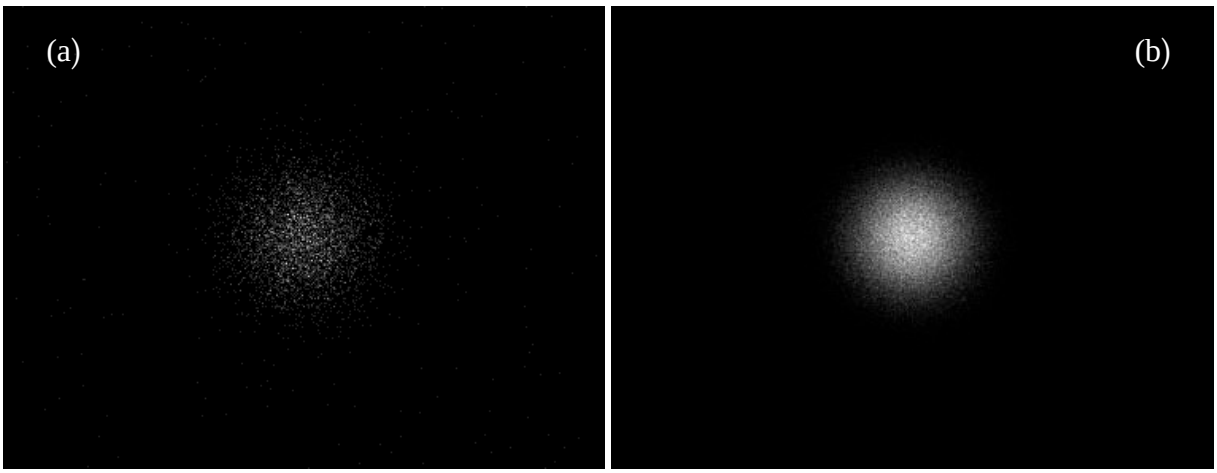

Figure 27. Simulated images of an ion bunch at injection, intensified to raise the brightest pixel to maximum. The integration time is (a) 20 ms and (b) 1 s.

projection. This calculation was repeated 2000 times to find the RMS error in the simulated beam-width measurement. The error for a single pilot bunch, in Table 3, is typically under 0.1%, except at energies where very small signals introduce noise into the fit.

The two noisy cases—a pilot bunch of protons at crossover (1.5-TeV) and lead ions at injection—have very few photoelectrons per turn in the peak pixel. Nevertheless, the errors are surprisingly small, because the camera integrates over 20 ms, and because the fit uses a projection rather than a single row or column through the peak. Despite the low photon count, the widths are found within 0.39% and 1.65% for the protons and ions respectively.

An image rather than a projection requires a larger signal per pixel. Even when the image intensifier raises the brightest pixel to the maximum value, a single injected bunch of lead ions produces the dim and noisy picture of Figure 27(a) when integrated over 20 ms. By lengthening the integration to 1 s, the peak pixel's photoelectron count reaches 70 with a standard deviation of 8.4; the intensified image is greatly improved (Figure 27(b)), although some noise is visible. An early ion fill, with 62 bunches, should form a similar image in 20 ms. Once the energy ramps to 1 TeV (equivalent), undulator light shifts from the infrared to the visible and provides more than enough light for good imaging of an ion bunch.

7.4 An Alternative for Bunch-by-Bunch Beam Profiles

In tests at the SPS, the Redlake has sometimes latched up in response to high radiation, and required power cycling to recover. Remote power cycling will be provided for the installation in the LHC, but the lifespan of this camera in the tunnel is hard to predict.

An alternative method to obtain bunch-by-bunch beam sizes, using measurements made over multiple turns was originally proposed for the synchrotron x-ray monitor for the positron beam of PEP-II [10]. The Redlake would be replaced with an opaque mask at the image of the beam. The mask has three narrow laser-cut slots, with widths of 20 μm ($\sigma/5$ at 7 TeV), that scan across the beam. Following the concept of a wire scanner, the slots are oriented horizontally, vertically, and at 45°, so that a photomultiplier (PMT) detecting the transmitted light measures three projections of the beam ellipse, in order to determine its major and minor axes and its tilt.

Every 25 ns (100 ns for ions), light from the image of another bunch arrives at the mask. The PMT signal is digitized and recorded in a matrix, with one column per bunch and one row for each consecutive LHC ring turn. The slot moves through the beam over many turns, with a

speed set to give 10 readings per σ of the bunch. Afterward, a Gaussian fit to each column gives the width of the projection of its bunch.

We calculated the number of photo-electrons produced at the PMT cathode as the horizontal slot (which finds the vertical profile) crosses the peak of a 7-TeV bunch. The light source is the dipole centre, and the best-resolution wavelength filter is used. The photomultiplier is a Hamamatsu R7400U-04, a small PMT with a 1-ns rise time, a fused-silica window, and response from 185 to 850 ns. The calculation found substantial signals: 7.8×10^5 photoelectrons from a nominal proton bunch, and 3.7×10^5 from an ion bunch. This is not surprising: since the slot width is comparable to a Proxicam pixel, the PMT signal should have similar intensity to the camera projections.

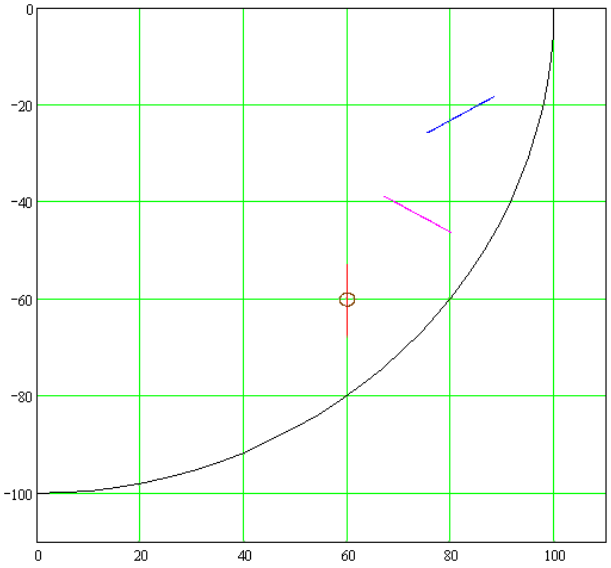

Figure 28. A rotating 100-mm-radius mask with three narrow slots. The vertical slot is crossing the image of the beam to find its profile along the *x* axis.

Instead of the piston-like linear motion of a wire scanner, it is more convenient to put the slots near the rim of a continuously rotating 100-mm-radius disc (Figure 28). An angle resolver on the motor provides the rotation angle (that is, the slot position) at the LHC ring-turn rate. A 0.25-Hz rotation rate scans the slot across the beam image at a suitable rate. With four sets of slots placed around the disc at 90° intervals, a new measurement of each of the 2808 bunches is available every second, using hardware that is simple and radiation resistant.

A prototype of the disc and motor is being prepared at SLAC in collaboration with Justin Albert of the University of Victoria in British Columbia, Canada. Digitization and processing can use the standard LHC electronics (DAB64x and IBMS) discussed in Section 8.2, but with modified firmware and software.

8 Abort-Gap Monitor

A 3-μs gap is provided in the fill pattern so that the abort-kicker magnets can rise from zero to full field without beam. After the rise, all particles in the ring are kicked into the dump line within one turn. Any particles inside the gap would pass through the kicker during its rise and receive a partial kick, insufficient for a clean extraction. Instead, their orbit perturbation could lead some to strike the Q4 quadrupole downstream of the extraction septum, causing Q4 to quench if the population is high enough. By constantly monitoring the gap, the beam can be aborted before this threshold population is reached. Monitoring is particularly important during fills, so that a bad fill can be halted and dumped before too much charge is misdirected into the gap.

The requirement [2] for the abort-gap monitor (AGM, also known as the BSRA) divides the 3-μs gap into 30 bins of 100 ns. In every 100-ms reporting interval, the number of particles per bin must be measured and compared with the threshold. Here we compute the signal from a threshold population in a bin and the expected error in this measurement.

8.1 Maximum Tolerable Proton and Lead-Ion Populations

The specification [2] sets the quench-threshold proton population at 4×10^{10} per 100-ns bin at injection, and 6×10^{7} per bin at 7 TeV; it requires the detection of 10% of these levels. A linear fit is arbitrarily suggested between these two values, but this is clearly unreasonable for a span of three orders of magnitude: it implies that a large proton population is tolerable up to energies near the maximum. The power-law fit ($\ln N$ linear in $\ln\gamma$) shown in Figure 29 seems more plausible.

The models used for beam-loss monitors provide a more rigorous estimate of quench thresholds. Bernd Dehning [11] provided a typical quench model, and Mariusz Sapinski then calculated quench thresholds versus proton energy specifically for Q4 [12]. Figure 29 includes these results. Both are similar, with end points more than an order of magnitude below those of the specification. Sapinski's end points are 1.1×10^{9} at 0.45 TeV and 1.8×10^{6} at 7 TeV.

In light of the quenches seen during beam tests in 2008, it is appropriate to adopt lower values, and so the fit to Sapinski's quench thresholds will be used below. We will compute the signal and signal-to-noise ratio of the AGM as a function of energy at the quench threshold and also consider whether 10% of this already reduced threshold can be detected.

A lost lead ion leaving the beampipe fragments as it hits the beam screen, and then deposits an amount of energy in a magnet coil comparable to that from Z lost protons at the equivalent stage of the energy ramp [13]. We thus set the threshold for ions at $1/Z$ times the quench limit for protons.

8.2 Instrumentation

Figure 9 shows a folding mirror between focusing mirrors F1 and F2. This is actually a beamsplitter, reflecting 90% for the imaging system and transmitting the rest for the AGM. A photomultiplier is placed at the intermediate image formed by F1 on the split path, since the diameter of the light there easily fits the 10-mm-diameter photocathode. Note that the light is picked off prior to the slit on the F1 focal plane. Thus the slit settings play no role in discriminating among sources for the AGM. All angles and sources that reflect from the extraction mirror are used. Blurring of the sources does not matter, since only a small diameter, but not an image, is needed for the PMT.

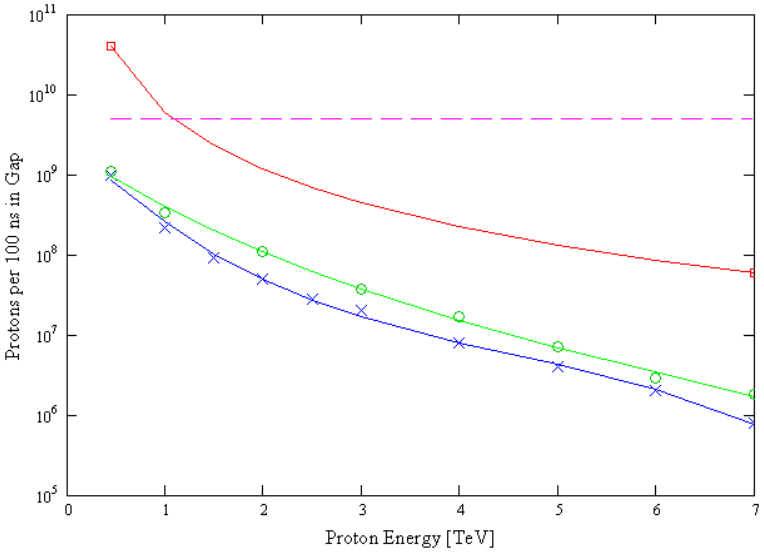

Figure 29. Proton population in the abort gap, per 100-ns interval, at quench threshold. Upper curve (red): the two points of the specification connected with a power-law fit. Middle curve (green): Sapinski's calculation with a fit. Lower curve (blue): Dehning's model with a fit. Sapinski's model is used here. Dashed line: Charge in a pilot bunch.

The PMT (Hamamatsu R5916-50) can be gated, since it uses a microchannel plate rather than dynodes. The gate allows the PMT to detect the small gap signal without saturating from the large population elsewhere. Figure 30 shows the PMT's spectral response, which extends into the ultraviolet, beyond the

reflectivity of the mirrors. The infrared cut-off is at 900 nm, limiting its sensitivity to the lead-ion spectrum at injection, as will be seen below.

The PMT has two important operating restrictions. The gate has a maximum duty cycle of 1%, limiting it to 900 ns per 89-μs turn. Instead, the gate is opened for the full 3-μs gap on every fourth turn (356 μs), for a duty cycle of 0.84%. Also, the maximum time-averaged anode current is 100 nA; with this duty cycle, the limit becomes 12 μA during the gate. This maximum is not reached with the weak light level expected at crossover, using maximum PMT gain. At other energies, the PMT gain must be lowered (or the light must be attenuated) to obey this limit.

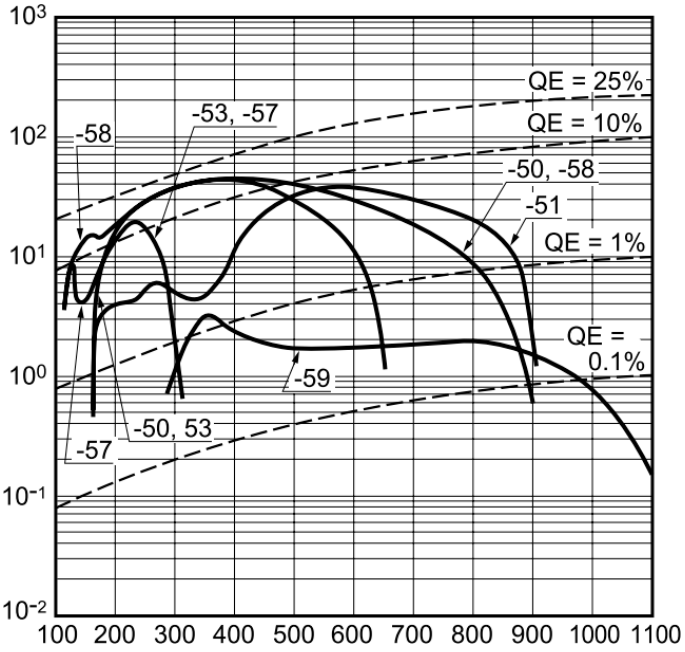

Figure 30. Radiant sensitivity (mA/W) of the Hamamatsu R5916-50 PMT (the "-50" curve) vs. wavelength (nm).

The PMT output is monitored by an IBMS charge-integrating board [14], which has a full-scale range of 60 pC. It is installed as a mezzanine card on the LHC Data Acquisition Board (DAB64x) [15]. Ideally, a particle population at the threshold should give a full-scale signal on the integrator, allowing good measurements of populations below threshold. However, the maximum PMT output of 12 μA integrates over a 100-ns bin to only 1.2 pC. An amplifier with a voltage gain of over 50 is necessary to allow for cable loss and to run the PMT below its limit. The Hamamatsu C5594, with a voltage gain of 63 (36 dB), was purchased for this purpose.

8.3 Monitoring Protons

The PMT's spectral response can be combined with the emission calculations to find the number of photoelectrons at the PMT's photocathode from a threshold population. Measurements in the 100-ns bins are summed over 100 ms (280 measurements, one every fourth turn) to find the reported output of the monitor, as shown in Table 4.

The table lists the PMT gain needed to fill the integrator to its maximum with a threshold population in the gap. The large variation in signal level over the ramp leads to large changes in the required gain. At crossover—1- and 1.5-TeV for protons—the gain would exceed the photomultiplier's limit of 1.05×10^6. We then restrict it to a maximum of 10^6, and cannot fill the integrator. Table 4 includes the corresponding high voltage (based on the nominal gain curve of the datasheet), the anode current, and the resulting charge in the integrator. The anode current approaches but does not exceed the 12 μA maximum.

Two noise sources are considered. Shot noise again follows a Poisson distribution with a mean equal to the expected photoelectron count in 100 ns, and a standard deviation equal to the square root of this number. The RMS noise of the electronics (PMT, amplifier, and IBMS) has been measured to be 130 counts of the 14-bit digitizer, which spans a range of ±60pC. The table lists both noise sources. They are then combined in quadrature to find the total noise and the noise-to-signal ratio.

Table 4. Signal from the abort-gap monitor versus beam energy, for protons and lead ions in a 100-ns bin, with the quench-threshold population in the gap. PMT gain and corresponding high voltage to fill the integrator (limited by PMT's maximum gain). Noise-to-signal ratio for sums over 100 ms and 1 s for the threshold population and for 10% of that population.

Beam Energy	**PMT**		**Signal in 100-ns at Quench Threshold**					**Noise/Signal of Multi-Turn Sum**			
	Gain	**Voltage**	**Photo-electrons**	**Anode Current**	**Charge**	**Shot Noise**	**Electr Noise**	**Threshold / 10**		**Threshold**	
TeV (equiv)								**100 ms**	**1 s**	**100 ms**	**1 s**
	×1000	*V*		*μA*	*pC*	*pC*	*pC*	*%*	*%*	*%*	*%*
Protons											
0.45	101.3	2883	64.48	10.5	60.00	7.47	0.95	2.54	0.80	0.75	0.24
1	1000.0	3351	1.34	2.1	12.28	10.62	0.95	16.99	5.37	5.19	1.64
1.5	1000.0	3351	2.25	3.6	20.65	13.77	0.95	12.90	4.08	4.00	1.26
2	106.0	2891	61.62	10.5	60.00	7.64	0.95	2.59	0.82	0.77	0.24
2.5	20.6	2666	317.54	10.5	60.00	3.37	0.95	1.42	0.45	0.35	0.11
3	11.5	2600	566.61	10.5	60.00	2.52	0.95	1.24	0.39	0.27	0.08
3.5	10.3	2587	635.19	10.5	60.00	2.38	0.95	1.21	0.38	0.26	0.08
4	9.6	2580	678.87	10.5	60.00	2.30	0.95	1.19	0.38	0.25	0.08
5	13.7	2619	475.63	10.5	60.00	2.75	0.95	1.28	0.41	0.29	0.09
6	20.9	2668	311.97	10.5	60.00	3.40	0.95	1.43	0.45	0.35	0.11
7	19.0	2656	344.50	10.5	60.00	3.23	0.95	1.39	0.44	0.34	0.11
Lead Ions											
0.45	1000.0	3351	0.43	0.7	3.91	5.99	0.95	32.44	10.26	9.28	2.94
1	80.8	2848	80.80	10.5	60.00	6.67	0.95	2.31	0.73	0.67	0.21
1.5	24.7	2688	264.48	10.5	60.00	3.69	0.95	1.50	0.47	0.38	0.12
2	1000.0	3351	6.02	9.6	55.27	22.53	0.95	7.77	2.46	2.44	0.77
2.5	1000.0	3351	4.85	7.8	44.54	20.23	0.95	8.68	2.74	2.72	0.86
3	1000.0	3351	6.01	9.6	55.24	22.53	0.95	7.78	2.46	2.44	0.77
3.5	659.8	3248	9.90	10.5	60.00	19.07	0.95	6.08	1.92	1.90	0.60
4	217.0	3014	30.09	10.5	60.00	10.94	0.95	3.57	1.13	1.09	0.35
5	20.5	2666	318.73	10.5	60.00	3.36	0.95	1.42	0.45	0.35	0.11
6	7.6	2554	863.31	10.5	60.00	2.04	0.95	1.15	0.36	0.22	0.07
7	4.1	2491	1577.68	10.5	60.00	1.51	0.95	1.06	0.34	0.18	0.06

The signal and noise are scaled appropriately for sums over both 100-ms and 1-s intervals, and for both 10% and 100% of the quench threshold. Table 4 lists the noise-to-signal ratio, which is below 5% for a population at 10% of the quench threshold for all cases except crossover; there it reaches 17%. However, recall that this threshold is over an order of magnitude below that proposed in the specification. Using a 1-s interval and 10% of threshold, or a 100-ms measurement at the full quench threshold, the ratio drops to 5%.

At crossover, the number of photoelectrons per bin at the quench threshold is barely above 1, and so the noise is comparable to the signal. At 10% of threshold, the noise in a bin exceeds the signal. A numerical simulation similar to that of Section 7.3 was performed to verify that the 100-ms and 1-s sums have an acceptable noise-to-signal ratio. The results agree precisely with the analytic approach of the previous paragraph. Meaningful statistics can be derived even from these especially weak signals.

8.4 Monitoring Lead Ions

Similar calculations for lead ions are shown in Table 4. At 10% of threshold, the noise-to-signal ratio for the 100-ms sum is below 9% at all energies except injection, where only 0.4 photoelectrons per bin are calculated to be emitted by the PMT, and so the ratio reaches 32%.

The injection spectrum is better suited to a mid-infrared detector, and the most suitable is HgCdTe, thermoelectrically cooled to −20 C. Smaller areas have lower noise, but we must consider a diameter of at least 1 mm to capture most of the beam, although this is only 2.6 times the RMS size (Table 1). However, even if *all* the light is used for the AGM rather than for imaging, this detector's dark current gives a calculated noise-to-signal ratio of 8.3.

Returning to the PMT, we see that at injection a 1-s sum detects 10% of threshold with a noise-to-signal ratio of 10%, and the full threshold can be found with 9% accuracy in 100 ms. These measurements should provide adequate safety.

8.5 Calibration

The calibration plan for the AGM compares the charge in each bin of the gap to the charge in an ordinary bunch. The Fast Beam-Current Transformer (FBCT) [16] measures the charge in every bunch using a fast transformer and an IBMS board. A high-gain input stage is used for pilot bunches.

The accuracy of the AGM calibration is limited by that of the FBCT. Tables 6 and 8 of the FBCT specification require an absolute calibration of the bunch charge to an RMS accuracy of:

- 1% of a nominal proton bunch = 1.1×10^9 protons;
- 10% of a pilot proton bunch = 5×10^8 protons;
- 10% of a nominal ion bunch = 7×10^6 ions.

Compare this demanding requirement to the quench thresholds:

- Protons: 1.1×10^9 at 0.45 TeV and 1.8×10^6 at 7 TeV;
- Ions: 1.4×10^7 at 0.45 TeV and 2.2×10^4 at 7 TeV (equivalent).

The FBCT is certainly not sensitive enough to monitor the abort gap. At injection, the accuracy of the calibration is equal to the quench threshold for protons, and only a factor of 2 below the quench threshold for ions. The thresholds then drop as the energy ramps, but the FBCT accuracy stays constant.

To calibrate the AGM, the PMT gate is delayed by 25 ns, so that the final 100-ns bin includes the first bunch. (If the only bunch in the ring is in a different time slot, the delay can be set accordingly.) The PMT gain is left unchanged. Calibrated optical attenuators are inserted into the light path to avoid an excessive PMT current and saturation of the integrator.

If, for example, a pilot bunch of 5×10^9 protons has been injected and stored, the AGM is calibrated by shifting the gate timing and inserting an optical attenuation of a factor of 5. The signal corresponds to $(5\times10^9 / 1.1\times10^9) / 5 = 91\%$ of the quench threshold. New calibrations are performed throughout the ramp as the threshold drops and the PMT gain is changed. At 7 TeV, an optical attenuation of 5000 gives a signal corresponding to $(5\times10^9 / 1.8\times10^6) / 3000 = 56\%$ of threshold. However, the error in the resulting calibration can be no better than the 10% measurement of the pilot bunch.

9 Conclusions

This Report computed the emission from the three sources of synchrotron light—the undulator, and the central and edge fields of the D3 dipole—that will measure the proton and lead-ion beams in the LHC. Analytic expressions for each were integrated over the geometric acceptance of the extraction mirror and over the spectral response of the optics and detectors,

for the full range of beam energies from injection to collisions (0.45 to 7 TeV for protons, and a factor of $Z = 82$ higher for the ions), in order to find the signals on the camera.

The optical system includes a long drift path in the vacuum chamber followed by an extraction mirror and a fused-silica window. An optical table including two focusing mirrors and cameras lies below the beamline. An "optical-trombone" delay line allows the focus to shift during the ramp from undulator to dipole.

For both protons and ions, the undulator is the only source contributing to measurements at low energy. As the energy ramps up, the undulator radiation in the camera's band falls off before the dipole radiation rises, causing a deep dip in available light. At the crossover point, where the undulator and dipole contributions are equal, some blurring of the image is to be expected as light is collected over a long path that runs from the centre of the undulator to the dipole entrance, 1 m away, and up to 3 m inside the dipole.

If the undulator remains on throughout the ramp, the blurring is transient as the dipole becomes far brighter than the undulator in the visible. Some manipulation of the focal-plane slit following the first focusing mirror can help to speed this transition, but the wide angular pattern of these sources at this energy does not allow a clean separation until the undulator light becomes insignificant. Turning off the undulator as the ramp passes the crossover energy would improve imaging there.

If left on at full energy, the undulator aims a fan of hard x rays (2.5 nm for 7 TeV protons) at the extraction mirror, but the total power is only 21 mW for protons (0.5 mW for ions), a small heat load that should not distort the mirror's surface.

At high proton energies, the angular spread of dipole edge radiation narrows to such an extent that diffractive blurring makes it unsuitable for measuring the proton beam. The spread for ions is wider and so is not a concern. Also, edge radiation is distinct from central radiation only when the measurement wavelengths are short compared to the critical wavelength in the dipole ($\lambda << \lambda_c$). For protons, this point is reached at 3 TeV, while for ions it occurs at 7.

Radiation from the central field of the dipole has emission angles that are sufficiently wide to avoid a large diffractive broadening of the measured beam size at 7 TeV. However, the image is affected by depth of field due to the long path in the dipole. An analysis including blurring from geometric optics, depth of field, and diffraction shows that central radiation at 400 nm from the first 2 m of the dipole broadens the image of 7-TeV protons by 17% vertically but by less than 1% horizontally, and provides the best balance of imaging and light collection.

The camera receives sufficient light for imaging protons and ions. However, even with the intensified camera, a good image of an ion bunch at injection needs a 1-s integration time. The other difficult situation, protons at crossover, provides somewhat more light.

A beamsplitter takes 10% of the light to monitor the abort gap with a gated photo-multiplier. This light appears to be adequate for measuring a quench-threshold population in the gap to 5% accuracy in 100 ms, even for the weak signals at crossover, but not for an ion beam at injection. Then the error is larger because the undulator spectrum is largely in the near infrared, but even in this case a threshold population can be measured to 9%. However, the accuracy of these measurements of the gap population is limited by a calibration comparing the AGM signal from the gap population to that from an ordinary bunch. Bunch charges are measured to an absolute accuracy of 1% for nominal bunches but only to 10% for proton pilot bunches or ion bunches.

References

1 L. Ponce, R. Jung and F. Méot, "LHC Proton Beam Diagnostics Using Synchrotron Radiation", CERN-2004-007.

2 C. Fischer, "High Sensitivity Measurement of the Longitudinal Distribution of the LHC Beams", LHC-B-ES-0005.00 rev. 2.0, EDMS 328145, https://edms.cern.ch/document/328145.

3 R. Maccaferri, M. Facchini, R. Jung, D. Tommasini and W. Venturini Delsolaro, "The 5-T Superconducting Undulator for the LHC Synchrotron Radiation Profile Monitor", LHC Project Report 731, EPAC, 5-9 July 2004, Lucerne, Switzerland.

4 Albert Hofmann, *The Physics of Synchrotron Radiation*, Cambridge University Press, (2004).

5 A. Thompson *et al*., *X-Ray Data Booklet*, LBNL/PUB-490, rev. 2 (2001).

6 R. Coïsson, "Angular-Spectral Distribution and Polarization of Synchrotron Radiation from a "Short" Magnet", Phys. Rev. A **20** (1979), pp. 524-528.

7 ZEMAX Development Corporation, http://www.zemax.com.

8 A.E. Siegman, *Lasers*, University Science Books (1986).

9 A.E. Siegman, "New developments in laser resonators", Proc. SPIE **1224**, p. 2 (1990).

10 A.S. Fisher, M. Ross, D. McCormick, K. Jobe, J.T. Seeman, H. DeStaebler, S. DeBarger, D. Kharakh, D. Arnett, M. Petree, B. Smith, J. Albert, D. Hitlin, J. Kadyk, J. Button-Shafer, "Design of an X-ray Imaging System for the Low-Energy Ring of PEP-II", EPAC, 5-9 July 2004, Lucerne, Switzerland.

11 B. Dehning, private communication.

12 M. Sapinski, private communication.

13 J.M. Jowett, "Ions in the LHC", CERN, Chamonix Workshop, 2009.

14 J.J. Savioz, "An Individual Bunch Measurement System for LHC Beam Instrumentation", LHC-B-ES-0010 ver. 1, EDMS 624344, https://edms.cern.ch/document/624344.

15 R. Jones, "VME64x Digital Acquisition Board for the LHC Trajectory and Closed Orbit System", LHC-BP-ES-0002 rev. 1.1, EDMS 410295, 2004-03-09, https://edms.cern.ch/document/410295.

16 C. Fischer and R. Schmidt, "On the Measurements of the Beam Current, Lifetime and Decay Rate in the LHC Rings", LHC-BCT-ES-0001 rev 1.0, EDMS 359172, 2005-01-17, https://edms.cern.ch/document/359172.